RANDPUNKT JOURNAL

Volume 1, Issue 1

First publication date: 2026-10-19

8 article(s) in this issue

ISSN: application pending (Reference No. 00009172)

Legal Notice

Publication title: RANDPUNKT JOURNAL

Publisher: Carlos Polanco González

Publication frequency: Monthly

Format: Electronic (online publication)

Language: English

First publication date: 2026-10-19

Website: https://randpunkt.org/

Publisher's address: Av. Contreras 270, col. San Jerónimo Lídice, C.P. 10200, Ciudad de México, México.

Contact: polanco@unam.mx

Exclusive Rights Reservation No.: 04-2026-102310350800-102

ISSN: application pending (Reference No. 00009172)

© **2026 RANDPUNKT JOURNAL.** All rights reserved, except for articles published under the Creative Commons Attribution 4.0 International (CC BY 4.0) license. Authors retain copyright in their individual contributions, which are published under CC BY 4.0 subject to the journal's publication terms.

Volume 1, Issue 1 — Table of Contents

First publication date: 2026-10-19

1. A Sparse Regression Framework for a Predictive Nomogram of Severe Low Anterior Resection Syndrome: Mathematical Foundations
Coral Leonor Blíe Magaña, María del Consuelo Díaz Romero — Short Note
DOI: 10.5281/zenodo.24167270

2. A Sparse Regression Framework for a Predictive Nomogram of Severe Low Anterior Resection Syndrome: Mathematical Foundations
Coral Leonor Blíe Magaña, María del Consuelo Díaz Romero — Short Note
DOI: 10.5281/zenodo.24167270

3. A Weighted Bipartite Network Framework for Quantifying Molecular Comorbidity: Application to Periodontal Disease
Mireya Martínez-García — Short Note
DOI: 10.5281/zenodo.24089234

4. Mathematical Structure of Exceptionally Compact Globular Proteins Containing a Large Internal Functional Cavity
Vladimir N. Uversky — Short Note
DOI: 10.5281/zenodo.24039999

5. A hybrid stochastic-deterministic operator framework for early detection of severe respiratory diseases with pandemic potential
Martha Rios Castro — Research Article
DOI: 10.5281/zenodo.24149964

6. Spiral RF Coil Analytical Modeling for Ultra-Low Field MRI Applications
Sergio Enrique Solís Nájera — Short Note
DOI: 10.5281/zenodo.24047654

7. A Mathematical Framework for Predicting the Location and Extent of Complex Cardiac Ruptures
Francisco Javier Roldan Gomez — Short Note
DOI: 10.5281/zenodo.24047363

8. Mathematical Structure of the Nonheme Iron Determination Assay
Alberto Huberman — Short Note
DOI: 10.5281/zenodo.24041134

A Sparse Regression Framework for a Predictive Nomogram of Severe Low Anterior Resection Syndrome: Mathematical Foundations

Coral Leonor Blíe Magaña, María del Consuelo Díaz Romero

Short Note

Received: 12 November 2026

Accepted: 12 November 2026

Published: 12 November 2026

DOI: 10.5281/zenodo.24167270

MSC 2020: 62J07

Published in RandPunkt Journal under the CC BY 4.0 license.

RandPunkt
Journal

ISSN 00009172 (Online)
APPLIED MATHEMATICS SERIES

A Sparse Regression Framework for a Predictive Nomogram of Severe Low Anterior Resection Syndrome: Mathematical Foundations

Coral Leonor Blé Magaña[1,*] **and María del Consuelo Díaz Romero**[1]

[1] *Instituto Nacional de Cancerología, Mexico City, Mexico*

[*] Correspondence to: **Coral Leonor Blé Magaña** ▪ blecoral@gmail.com

Volume 1, Issue 1, 2026 **Pages:** [1 – 3] ▪ 3 pages
Published on: 12 November 2026 Article DOI: 10.5281/zenodo.24167270

Severe low anterior resection syndrome (LARS) is a major functional sequel of colorectal cancer treatment, and current clinical practice lacks predictive models that allow early stratification of patients at risk. This note argues that the appropriate mathematical framework is not a hand-crafted risk score but a sparse logistic regression with structured regularization. We formalize the problem as the estimation of a sparse coefficient vector in a generalized linear model and identify the mathematical objects involved: a design matrix with block-structured covariates, a logistic loss with an ℓ_1 or ℓ_1/ℓ_2 penalty, and a nomogram as a monotone transformation of the fitted linear predictor. We prove a proposition establishing that, under the weighting $w_g = \sqrt{|g|}$ and singleton blocks, the group-Lasso formulation reduces to the standard Lasso, thereby unifying the two regularization paths and justifying the use of block penalties for clinically meaningful covariate groups. The framework is instantiated on a retrospective cohort of colorectal cancer patients treated at the Instituto Nacional de Cancerología (INCan) in Mexico City, with clinically defined covariate blocks (neoadjuvant therapy, radiotherapy, type of surgery, hip adductor strength, continence status, time since surgery). The result provides a rigorous foundation for the nomogram as a calibrated decision tool in multidisciplinary prehabilitation.

Keywords: Lasso; group Lasso; logistic regression; nomogram; low anterior resection syndrome; penalized likelihood; statistical learning.

Received: 10 November 2026 ▪ Accepted: 11 November 2026 ▪ Published: 12 November 2026© 2026 CC by ▪ 4.0v

1 The statistical object

Let $Y \in \{0, 1\}$ indicate severe LARS and let $\{(\mathbf{x}_i, Y_i)\}_{i=1}^n$ be a cohort with covariates $\mathbf{x}_i \in \mathbb{R}^p$ (clinical, oncological, and surgical variables). The model is the logistic regression

$$\mathbb{P}(Y = 1 \mid \mathbf{x}) = \sigma(\eta(\mathbf{x})) = \frac{1}{1 + e^{-\eta(\mathbf{x})}}, \tag{1}$$

with linear predictor $\eta(\mathbf{x}) = \beta_0 + \mathbf{x}^\top \beta$. The parameter $\beta \in \mathbb{R}^p$ is estimated by minimizing the negative log-likelihood with an ℓ_1 penalty,

$$\widehat{\beta}(\lambda) = \arg\min_{\beta \in \mathbb{R}^p} \left\{ -\frac{1}{n} \sum_{i=1}^{n} \Big[Y_i \log \sigma(\eta_i) + (1 - Y_i) \log \big(1 - \sigma(\eta_i)\big) \Big] + \lambda \|\beta\|_1 \right\}, \tag{2}$$

where $\lambda \geq 0$ is the regularization parameter. This is the standard Lasso-logistic formulation for sparse variable selection in clinical prediction [1, 2].

The nomogram is obtained as a monotone transformation of $\widehat{\eta}(\mathbf{x})$: each covariate contributes a number of points proportional to $|\widehat{\beta}_j x_j|$, and the total points map to a predicted probability through the inverse logistic function (1). This is the graphical representation of the same mathematical object, not a different model [3].

2 Block structure and the group penalty

The covariates in the LARS problem fall into clinically meaningful blocks: treatment-related variables (neoadjuvant therapy, radiotherapy, type of surgery), functional variables (hip adductor strength, continence status), and temporal variables (time since surgery, evolution of incontinence). Two distinct effects must be separated here.

First, *scale*. Without standardization, a plain Lasso on raw covariates is dominated by variables with large numeric range. This effect is removed by the standardization described in Section 4.

Second, *block selection*. After standardization, the ℓ_1 penalty still treats each dummy level of a categorical factor independently, so it may select isolated levels rather than entire factors. This second failure mode is not removed by standardization and is the one the group penalty addresses [4].

The group-Lasso replaces the ℓ_1 penalty in (2) by a sum of ℓ_2 norms over pre-specified blocks,

$$\widehat{\beta}(\lambda) = \arg\min_{\beta} \left\{ -\ell(\beta) + \lambda \sum_{g=1}^{G} w_g \|\beta_g\|_2 \right\}, \tag{3}$$

where β_g is the sub-vector of coefficients in block g, $w_g > 0$ is a block-specific weight, and $\ell(\beta)$ is the log-likelihood in (2). The penalty $\sum_g w_g \|\beta_g\|_2$ encourages entire blocks to be zero, which matches the clinical requirement that whole factors be selected or discarded [4].

This formulation is naturally suited to the target of a 3–4 variable nomogram. The regularization path $\lambda \mapsto \widehat{\beta}(\lambda)$ selects a nested sequence of sparse models; the value of λ chosen by cross-validation determines the number of active covariates, and the target model size corresponds to a specific point on this path rather than to a property of the penalty itself.

3 A consistency relation between group-Lasso and Lasso

The following proposition establishes that the group-Lasso contains the standard Lasso as a special case, providing a bridge between the two formulations.

Proposition 3.1. *Let the blocks be singletons, $g_j = \{j\}$ for $j = 1, \ldots, p$, and set $w_g = \sqrt{|g|}$ for each block g. Then the group-Lasso problem (3) coincides with the Lasso problem (2).*

Proof. With singleton blocks, $\beta_{g_j} = \beta_j \in \mathbb{R}$ and $\|\beta_{g_j}\|_2 = |\beta_j|$. The weight is $w_{g_j} = \sqrt{|\{j\}|} = 1$. Therefore

$$\sum_{g=1}^{G} w_g \|\beta_g\|_2 = \sum_{j=1}^{p} 1 \cdot |\beta_j| = \|\beta\|_1.$$

Substituting into (3) yields exactly (2). □

Remark 3.2. Proposition 3.1 shows that the group penalty is a strict generalization of the ℓ_1 penalty, not a different regularization principle. The choice $w_g = \sqrt{|g|}$ is the standard scaling that makes the group penalty comparable across blocks of different sizes [4]. In the LARS application, where blocks have sizes 2–5, this weighting prevents large blocks from being penalized disproportionately.

Remark 3.3. For the logistic loss, non-asymptotic oracle inequalities for both the Lasso and the group-Lasso have been established under restricted eigenvalue conditions [5]. These results provide the theoretical justification for using cross-validated λ as a data-driven selector of the number of active covariates, which in turn determines the size of the nomogram.

4 Computational realization

The estimation proceeds by coordinate descent on (3), with the regularization path computed on a grid of λ values and λ selected by k-fold cross-validation [2]. The design matrix uses one-hot encoding for categorical variables and standardization for continuous variables, so that the penalty acts on comparable scales.

Performance is assessed by discrimination (area under the ROC curve) and calibration (calibration slope, Brier score). Internal validity is estimated by bootstrap optimism correction. The nomogram is constructed from the fitted linear predictor, with point scales for each selected block and a total-points-to-probability conversion table.

Penalized regression has been widely adopted in oncological nomogram construction because it produces sparse, interpretable models [3]; the trade-off between predictive accuracy and interpretability is documented in that literature. The Lasso formulation extends that practice into a principled variable-selection framework, in which the number of predictors is not chosen by hand but by the regularization path.

5 Outlook

The framework is not a hand-crafted risk score: it is a penalized likelihood problem on a structured covariate space. Its mathematical content is the reduction relation of Proposition 3.1 and the regularization path that selects the nomogram. The clinical variables that enter the model are the same ones identified in prior work on functional outcomes after colorectal surgery, but their role here is mathematical: they

define the block structure of the penalty. The output is a calibrated probability of severe LARS together with an interpretable nomogram suitable for multidisciplinary prehabilitation decisions.

The clinical instantiation of this framework is a retrospective cohort of patients with colorectal cancer treated at the Instituto Nacional de Cancerología (INCan) in Mexico City. The covariate blocks are defined by the variables that the clinical protocol identifies as relevant: treatment-related variables (neoadjuvant therapy, radiotherapy, type of surgery), functional variables (hip adductor strength, continence status), and temporal variables (time since surgery, evolution of incontinence). Confounding variables identified in prior work, such as diet, concomitant medication, and time of evolution of incontinence, enter the design matrix as additional blocks and are subject to the same group penalty. The target of 3–4 active variables reported in the protocol corresponds, as discussed in Section 2, to a specific point on the regularization path selected by cross-validation.

The clinical utility of the resulting nomogram is twofold. First, it allows the multidisciplinary team—colorectal surgery, medical oncology, and oncologic physiotherapy—to identify at diagnosis those patients at high risk of severe bowel dysfunction, before the functional sequel becomes clinically manifest. Second, it provides a quantitative justification for initiating pelvic-floor prehabilitation and rehabilitation protocols in a timely and personalized manner, rather than uniformly across the cohort. From the mathematical standpoint, the nomogram is a calibrated probability map on the covariate space; from the clinical standpoint, it is a decision instrument that converts that probability into a prehabilitation trigger. The two readings are not in tension: they are the same object observed from two disciplines.

References

[1] Tibshirani, R., *Regression Shrinkage and Selection via the Lasso*, Journal of the Royal Statistical Society: Series B (Methodological) 58.**1** (1996), pp. 267–288, doi:10.1111/j.2517-6161.1996.tb02080.x.

[2] Friedman, J., Hastie, T., and Tibshirani, R., *Regularization Paths for Generalized Linear Models via Coordinate Descent*, Journal of Statistical Software 33.**1** (2010), pp. 1–22, doi:10.18637/jss.v033.i01.

[3] Iasonos, A., Schrag, D., Raj, G. V., and Panageas, K. S., *How To Build and Interpret a Nomogram for Cancer Prognosis*, Journal of Clinical Oncology 26.**8** (2008), pp. 1364–1370, doi:10.1200/JCO.2007.12.9791.

[4] Yuan, M. and Lin, Y., *Model Selection and Estimation in Regression with Grouped Variables*, Journal of the Royal Statistical Society: Series B (Statistical Methodology) 68.**1** (2006), pp. 49–67, doi:10.1111/j.1467-9868.2005.00532.x.

[5] Bach, F., *Self-concordant analysis for logistic regression*, Electronic Journal of Statistics 4 (2010), pp. 384–414, doi:10.1214/09-EJS521.

A Sparse Regression Framework for a Predictive Nomogram of Severe Low Anterior Resection Syndrome: Mathematical Foundations

Coral Leonor Blíe Magaña, María del Consuelo Díaz Romero

Short Note

Received: 10 November 2026

Accepted: 11 November 2026

Published: 12 November 2026

DOI: 10.5281/zenodo.24167270

MSC 2020: 62J07

Published in RandPunkt Journal under the CC BY 4.0 license.

RandPunkt
Journal

ISSN 00009172 (Online)
APPLIED MATHEMATICS SERIES

A Sparse Regression Framework for a Predictive Nomogram of Severe Low Anterior Resection Syndrome: Mathematical Foundations

Coral Leonor Blé Magaña[1,*] **and María del Consuelo Díaz Romero**[1]

[1] *Instituto Nacional de Cancerología, Mexico City, Mexico*

[*] Correspondence to: **Coral Leonor Blé Magaña** ▪ blecoral@gmail.com

Volume 1, Issue 1, 2026 **Pages:** [1 – 3] ▪ 3 pages
Published on: 12 November 2026 Article DOI: 10.5281/zenodo.24167270

Severe low anterior resection syndrome (LARS) is a major functional sequel of colorectal cancer treatment, and current clinical practice lacks predictive models that allow early stratification of patients at risk. This note argues that the appropriate mathematical framework is not a hand-crafted risk score but a sparse logistic regression with structured regularization. We formalize the problem as the estimation of a sparse coefficient vector in a generalized linear model and identify the mathematical objects involved: a design matrix with block-structured covariates, a logistic loss with an ℓ_1 or ℓ_1/ℓ_2 penalty, and a nomogram as a monotone transformation of the fitted linear predictor. We prove a proposition establishing that, under the weighting $w_g = \sqrt{|g|}$ and singleton blocks, the group-Lasso formulation reduces to the standard Lasso, thereby unifying the two regularization paths and justifying the use of block penalties for clinically meaningful covariate groups. The framework is instantiated on a retrospective cohort of colorectal cancer patients treated at the Instituto Nacional de Cancerología (INCan) in Mexico City, with clinically defined covariate blocks (neoadjuvant therapy, radiotherapy, type of surgery, hip adductor strength, continence status, time since surgery). The result provides a rigorous foundation for the nomogram as a calibrated decision tool in multidisciplinary prehabilitation.

Keywords: Lasso; group Lasso; logistic regression; nomogram; low anterior resection syndrome; penalized likelihood; statistical learning.

Received: 10 November 2026 ▪ Accepted: 11 November 2026 ▪ Published: 12 November 2026© 2026 CC by ▪ 4.0v

1 The statistical object

Let $Y \in \{0, 1\}$ indicate severe LARS and let $\{(\mathbf{x}_i, Y_i)\}_{i=1}^n$ be a cohort with covariates $\mathbf{x}_i \in \mathbb{R}^p$ (clinical, oncological, and surgical variables). The model is the logistic regression

$$\mathbb{P}(Y = 1 \mid \mathbf{x}) = \sigma(\eta(\mathbf{x})) = \frac{1}{1 + e^{-\eta(\mathbf{x})}}, \tag{1}$$

with linear predictor $\eta(\mathbf{x}) = \beta_0 + \mathbf{x}^\top \beta$. The parameter $\beta \in \mathbb{R}^p$ is estimated by minimizing the negative log-likelihood with an ℓ_1 penalty,

$$\widehat{\beta}(\lambda) = \arg\min_{\beta \in \mathbb{R}^p} \left\{ -\frac{1}{n} \sum_{i=1}^{n} \Big[Y_i \log \sigma(\eta_i) + (1 - Y_i) \log \big(1 - \sigma(\eta_i)\big) \Big] + \lambda \|\beta\|_1 \right\}, \tag{2}$$

where $\lambda \geq 0$ is the regularization parameter. This is the standard Lasso-logistic formulation for sparse variable selection in clinical prediction [1, 2].

The nomogram is obtained as a monotone transformation of $\widehat{\eta}(\mathbf{x})$: each covariate contributes a number of points proportional to $|\widehat{\beta}_j x_j|$, and the total points map to a predicted probability through the inverse logistic function (1). This is the graphical representation of the same mathematical object, not a different model [3].

2 Block structure and the group penalty

The covariates in the LARS problem fall into clinically meaningful blocks: treatment-related variables (neoadjuvant therapy, radiotherapy, type of surgery), functional variables (hip adductor strength, continence status), and temporal variables (time since surgery, evolution of incontinence). Two distinct effects must be separated here.

First, *scale*. Without standardization, a plain Lasso on raw covariates is dominated by variables with large numeric range. This effect is removed by the standardization described in Section 4.

Second, *block selection*. After standardization, the ℓ_1 penalty still treats each dummy level of a categorical factor independently, so it may select isolated levels rather than entire factors. This second failure mode is not removed by standardization and is the one the group penalty addresses [4].

The group-Lasso replaces the ℓ_1 penalty in (2) by a sum of ℓ_2 norms over pre-specified blocks,

$$\widehat{\beta}(\lambda) = \arg\min_{\beta} \left\{ -\ell(\beta) + \lambda \sum_{g=1}^{G} w_g \|\beta_g\|_2 \right\}, \tag{3}$$

where β_g is the sub-vector of coefficients in block g, $w_g > 0$ is a block-specific weight, and $\ell(\beta)$ is the log-likelihood in (2). The penalty $\sum_g w_g \|\beta_g\|_2$ encourages entire blocks to be zero, which matches the clinical requirement that whole factors be selected or discarded [4].

This formulation is naturally suited to the target of a 3–4 variable nomogram. The regularization path $\lambda \mapsto \widehat{\beta}(\lambda)$ selects a nested sequence of sparse models; the value of λ chosen by cross-validation determines the number of active covariates, and the target model size corresponds to a specific point on this path rather than to a property of the penalty itself.

3 A consistency relation between group-Lasso and Lasso

The following proposition establishes that the group-Lasso contains the standard Lasso as a special case, providing a bridge between the two formulations.

Proposition 3.1. *Let the blocks be singletons, $g_j = \{j\}$ for $j = 1, \ldots, p$, and set $w_g = \sqrt{|g|}$ for each block g. Then the group-Lasso problem (3) coincides with the Lasso problem (2).*

Proof. With singleton blocks, $\beta_{g_j} = \beta_j \in \mathbb{R}$ and $\|\beta_{g_j}\|_2 = |\beta_j|$. The weight is $w_{g_j} = \sqrt{|\{j\}|} = 1$. Therefore

$$\sum_{g=1}^{G} w_g \|\beta_g\|_2 = \sum_{j=1}^{p} 1 \cdot |\beta_j| = \|\beta\|_1.$$

Substituting into (3) yields exactly (2). □

Remark 3.2. Proposition 3.1 shows that the group penalty is a strict generalization of the ℓ_1 penalty, not a different regularization principle. The choice $w_g = \sqrt{|g|}$ is the standard scaling that makes the group penalty comparable across blocks of different sizes [4]. In the LARS application, where blocks have sizes 2–5, this weighting prevents large blocks from being penalized disproportionately.

Remark 3.3. For the logistic loss, non-asymptotic oracle inequalities for both the Lasso and the group-Lasso have been established under restricted eigenvalue conditions [5]. These results provide the theoretical justification for using cross-validated λ as a data-driven selector of the number of active covariates, which in turn determines the size of the nomogram.

4 Computational realization

The estimation proceeds by coordinate descent on (3), with the regularization path computed on a grid of λ values and λ selected by k-fold cross-validation [2]. The design matrix uses one-hot encoding for categorical variables and standardization for continuous variables, so that the penalty acts on comparable scales.

Performance is assessed by discrimination (area under the ROC curve) and calibration (calibration slope, Brier score). Internal validity is estimated by bootstrap optimism correction. The nomogram is constructed from the fitted linear predictor, with point scales for each selected block and a total-points-to-probability conversion table.

Penalized regression has been widely adopted in oncological nomogram construction because it produces sparse, interpretable models [3]; the trade-off between predictive accuracy and interpretability is documented in that literature. The Lasso formulation extends that practice into a principled variable-selection framework, in which the number of predictors is not chosen by hand but by the regularization path.

5 Outlook

The framework is not a hand-crafted risk score: it is a penalized likelihood problem on a structured covariate space. Its mathematical content is the reduction relation of Proposition 3.1 and the regularization path that selects the nomogram. The clinical variables that enter the model are the same ones identified in prior work on functional outcomes after colorectal surgery, but their role here is mathematical: they

define the block structure of the penalty. The output is a calibrated probability of severe LARS together with an interpretable nomogram suitable for multidisciplinary prehabilitation decisions.

The clinical instantiation of this framework is a retrospective cohort of patients with colorectal cancer treated at the Instituto Nacional de Cancerología (INCan) in Mexico City. The covariate blocks are defined by the variables that the clinical protocol identifies as relevant: treatment-related variables (neoadjuvant therapy, radiotherapy, type of surgery), functional variables (hip adductor strength, continence status), and temporal variables (time since surgery, evolution of incontinence). Confounding variables identified in prior work, such as diet, concomitant medication, and time of evolution of incontinence, enter the design matrix as additional blocks and are subject to the same group penalty. The target of 3–4 active variables reported in the protocol corresponds, as discussed in Section 2, to a specific point on the regularization path selected by cross-validation.

The clinical utility of the resulting nomogram is twofold. First, it allows the multidisciplinary team—colorectal surgery, medical oncology, and oncologic physiotherapy—to identify at diagnosis those patients at high risk of severe bowel dysfunction, before the functional sequel becomes clinically manifest. Second, it provides a quantitative justification for initiating pelvic-floor prehabilitation and rehabilitation protocols in a timely and personalized manner, rather than uniformly across the cohort. From the mathematical standpoint, the nomogram is a calibrated probability map on the covariate space; from the clinical standpoint, it is a decision instrument that converts that probability into a prehabilitation trigger. The two readings are not in tension: they are the same object observed from two disciplines.

References

[1] Tibshirani, R., *Regression Shrinkage and Selection via the Lasso*, Journal of the Royal Statistical Society: Series B (Methodological) 58.**1** (1996), pp. 267–288, doi:10.1111/j.2517-6161.1996.tb02080.x.

[2] Friedman, J., Hastie, T., and Tibshirani, R., *Regularization Paths for Generalized Linear Models via Coordinate Descent*, Journal of Statistical Software 33.**1** (2010), pp. 1–22, doi:10.18637/jss.v033.i01.

[3] Iasonos, A., Schrag, D., Raj, G. V., and Panageas, K. S., *How To Build and Interpret a Nomogram for Cancer Prognosis*, Journal of Clinical Oncology 26.**8** (2008), pp. 1364–1370, doi:10.1200/JCO.2007.12.9791.

[4] Yuan, M. and Lin, Y., *Model Selection and Estimation in Regression with Grouped Variables*, Journal of the Royal Statistical Society: Series B (Statistical Methodology) 68.**1** (2006), pp. 49–67, doi:10.1111/j.1467-9868.2005.00532.x.

[5] Bach, F., *Self-concordant analysis for logistic regression*, Electronic Journal of Statistics 4 (2010), pp. 384–414, doi:10.1214/09-EJS521.

A Weighted Bipartite Network Framework for Quantifying Molecular Comorbidity: Application to Periodontal Disease

Mireya Martínez-García

Short Note

Received: 09 November 2026

Accepted: 09 November 2026

Published: 09 November 2026

DOI: 10.5281/zenodo.24089234

MSC 2020: 05C90

Published in RandPunkt Journal under the CC BY 4.0 license.

RandPunkt
Journal

ISSN 00009172 (Online)
APPLIED MATHEMATICS SERIES

A Weighted Bipartite Network Framework for Quantifying Molecular Comorbidity: Application to Periodontal Disease

Mireya Martínez-García[1]

[1] *Dental Public Health Department, Division of Graduate Studies and Research, School of Dentistry, Universidad Nacional Autónoma de México, Mexico City 04510, Mexico*

*Correspondence to: **Mireya Martínez-García** ▪ mireya.martinez@fo.odonto.unam.mx

Volume 1, Issue 1, 2026
Published on: 8 November 2026

Pages: [1–8] ▪ 8 pages
Article DOI: 10.5281/zenodo.24089234

Abstract. The mathematical formalisms underlying disease–gene overlap metrics in network medicine remain largely implicit. We formalize the disease–gene relation as a weighted bipartite graph represented by a biadjacency matrix $\mathbf{W}$, with edge weights combining DisGeNET confidence scores and pLI values, and derive a pLI-weighted Jaccard coefficient J_w and a hub centrality index H. We establish three formal results: boundedness and reduction to the classical Jaccard index (Proposition 1), strict refinement of the classical index (Proposition 2), and non-metricity of the induced dissimilarity, so comorbidity is not transitive (Proposition 3). We further show that $H = \mathbf{W}^{\top}\mathbf{k}$ is bounded by the leading singular value of $\mathbf{W}$ and derive a perturbation bound for the stability of the hub ranking. The formalism is illustrated on the periodontal diseasome of Martínez-García and Hernández-Lemus (2024): that study provided the dataset and the biological interpretation; the present note provides the formal structure, the three propositions, and the spectral and perturbation bounds, none of which were considered there. TNF and IL6 achieve the highest centrality ($H = 24$ and 23), and J_w discriminates comorbidity pairs that classical Jaccard treats as equivalent.

Keywords: molecular comorbidity • bipartite networks • weighted Jaccard index • hub centrality • spectral bounds • periodontal disease • network medicine

Received: 25 October 2026 ▪ Accepted: 3 November 2026 ▪ Published: 8 November 2026 © 2026 CC by ▪ 4.0v

1 Setting and main result

Network-based analyses of human disease — the so-called diseasome — have consistently revealed that conditions sharing molecular components tend to co-occur in patients [1, 2, 3]. Periodontal disease is a particularly instructive case: its systemic associations with cardiovascular disease, type 2 diabetes, rheumatoid arthritis, Alzheimer's disease, and several cancers are now well documented [4, 5, 6], and a recent comprehensive analysis [7] mapped its full molecular comorbidity network using DisGeNET2R, identifying 2,219 curated gene–disease interactions across 80 conditions. A limitation shared by that and most other diseasome studies is that the mathematical formalism underlying the overlap metrics is left implicit: the Jaccard index treats all shared genes as equally informative regardless of phenotypic impact, and the designation of "hub gene" remains descriptive rather than formally justified.

The present note is derived from the study of Martínez-García and Hernández-Lemus [7]. That study reported the molecular comorbidity network of periodontal disease, including the 2,219 curated gene–disease interactions and the eleven hub genes that we use here. It did not, however, formalize the mathematical structure underlying the overlap metrics it employed descriptively: the Jaccard index was used as a set-overlap measure without weights, and the hub designation was based on degree alone. The present note takes the published dataset of [7] as input and asks a different question: what formal structure underlies the disease–gene overlap when the associations are weighted by phenotypic impact? We formalize the disease–gene relation as a weighted bipartite graph represented by a non-negative biadjacency matrix $\mathbf{W}$, derive a pLI-weighted Jaccard coefficient J_w, and define a hub centrality index H. We prove three propositions establishing the formal properties of J_w, show that H admits a spectral representation bounded by the leading singular value of $\mathbf{W}$, and derive a perturbation bound for the stability of the hub ranking. These results — the matrix representation, the three propositions, the spectral bound, and the perturbation analysis — are new and were not considered in [7]. The periodontal application in Section 3 is an illustration of the formalism on the published dataset, not a report of new biological data.

2 The formalism

2.1 Graph and matrix

Let $D = \{d_1, d_2, \ldots, d_m\}$ be a finite set of diseases and $\Gamma = \{\gamma_1, \gamma_2, \ldots, \gamma_n\}$ be a finite set of genes. Define a bipartite graph

$$G = (D \cup \Gamma,\ E,\ w), \tag{1}$$

where $E \subseteq D \times \Gamma$ is the edge set and $w : E \to \mathbb{R}^+$ is a weight function. An edge $(d_i, \gamma_j) \in E$ exists if and only if gene γ_j has a curated association with disease d_i in a gene–disease association database such as DisGeNET [8]. The edge weight is

$$w_{ij} = \mathrm{pLI}(\gamma_j) \cdot c_{ij}, \tag{2}$$

where $\mathrm{pLI}(\gamma_j) \in [0, 1]$ is the probability of loss-of-function intolerance of gene γ_j, derived from large-scale sequencing data (e.g., the Genome Aggregation Database, gnomAD) [9], and $c_{ij} \in [0, 1]$ is the DisGeNET confidence score for the (d_i, γ_j) association [8]. High pLI indicates that loss-of-function variants in γ_j are strongly deleterious, conferring phenotypic weight to its associations.

Equivalently, G admits a biadjacency matrix representation $\mathbf{W} \in \mathbb{R}^{m \times n}$ with entries

$$W_{ij} = \begin{cases} w_{ij}, & (d_i, \gamma_j) \in E, \\ 0, & \text{otherwise}, \end{cases} \tag{3}$$

so that the gene neighborhood of d_i is the support of row i, $\Gamma(d_i) = \mathrm{supp}(\mathbf{W}_{i\cdot})$, and the disease neighborhood of γ_j is the support of column j, $\Gamma^{-1}(\gamma_j) = \mathrm{supp}(\mathbf{W}_{\cdot j})$. The degree sequences are then $k(d_i) = \|\mathbf{W}_{i\cdot}\|_0$ and $\deg(\gamma_j) = \|\mathbf{W}_{\cdot j}\|_0$, where $\|\cdot\|_0$ denotes the ℓ_0 pseudonorm. The map $\mathbf{W} \mapsto G$ is a bijection between weighted bipartite graphs on $D \times \Gamma$ and non-negative matrices of that shape. All functionals introduced below are therefore functionals on $\mathbf{W}$, and we shall move freely between the graph-theoretic and matrix-theoretic descriptions. The classical unweighted diseasome of Goh et al. [1] corresponds to the special case $w_{ij} = 1$ for all $(d_i, \gamma_j) \in E$, i.e. to the 0/1 biadjacency matrix $\mathbf{A} = \mathbb{1}[\mathbf{W} > 0]$; the present formulation thus strictly generalizes prior work.

2.2 Weighted similarity and its properties

The standard Jaccard similarity between two diseases d_a and d_b is

$$J(d_a, d_b) = \frac{|\Gamma(d_a) \cap \Gamma(d_b)|}{|\Gamma(d_a) \cup \Gamma(d_b)|}. \tag{4}$$

This treats all shared genes identically. To incorporate phenotypic relevance, we define the pLI-weighted Jaccard coefficient

$$J_w(d_a, d_b) = \frac{\displaystyle\sum_{\gamma \in \Gamma(d_a) \cap \Gamma(d_b)} w_{a\gamma} \cdot w_{b\gamma}}{\displaystyle\sum_{\gamma \in \Gamma(d_a) \cup \Gamma(d_b)} \max(w_{a\gamma},\, w_{b\gamma})}, \tag{5}$$

where $w_{a\gamma} = 0$ if $\gamma \notin \Gamma(d_a)$ (and analogously for b). Equation (5) can be written more transparently as a min-over-max ratio,

$$J_w(d_a, d_b) = \frac{\displaystyle\sum_{\gamma=1}^{n} \min(w_{a\gamma}, w_{b\gamma})\, \mathbb{1}[\gamma \in \Gamma(d_a) \cap \Gamma(d_b)]}{\displaystyle\sum_{\gamma=1}^{n} \max(w_{a\gamma}, w_{b\gamma})\, \mathbb{1}[\gamma \in \Gamma(d_a) \cup \Gamma(d_b)]}, \tag{6}$$

which exhibits J_w as a comparison-dependent normalized overlap: unlike the classical Jaccard ratio, it is not induced by a fixed metric on $\mathbb{R}^n$, a point made precise in Proposition 3.

Proposition 1 (Bounds and reduction). For all disease pairs (d_a, d_b): (i) $0 \le J_w(d_a, d_b) \le 1$; (ii) $J_w(d_a, d_b) = 1$ if and only if $\Gamma(d_a) = \Gamma(d_b)$ and $w_{a\gamma} = w_{b\gamma}$ for all γ; (iii) when $w_{ij} = c$ for all $(i, j) \in E$ (uniform weights), J_w reduces to the classical J.

Proof sketch. (i) Follows from non-negativity of w and the inequality numerator $\le$ denominator by construction (Cauchy–Schwarz applied to the product form in the numerator vs. the max in the denominator). (ii) Equality holds iff numerator = denominator, which requires identical neighborhoods with identical weights. (iii) Substituting c yields $|\Gamma(d_a) \cap \Gamma(d_b)| \cdot c^2$ in the numerator and $|\Gamma(d_a) \cup \Gamma(d_b)| \cdot c$ in the denominator; the ratio simplifies to $J(d_a, d_b) \cdot c$, normalized to J when $c = 1$. □

Proposition 2 (Discriminating power). There exist disease pairs (d_a, d_b) and (d_a, d_c) such that $J(d_a, d_b) = J(d_a, d_c)$ but $J_w(d_a, d_b) \neq J_w(d_a, d_c)$.

Proof. Let $|\Gamma(d_a) \cap \Gamma(d_b)| = |\Gamma(d_a) \cap \Gamma(d_c)| = k$ and $|\Gamma(d_a) \cup \Gamma(d_b)| = |\Gamma(d_a) \cup \Gamma(d_c)| = K$, so $J(d_a, d_b) = J(d_a, d_c) = k/K$. If the k shared genes with d_b have high pLI $\times\, c$ (close to 1) while those with d_c have low values, then $\sum_\gamma w_{a\gamma} w_{b\gamma} \gg \sum_\gamma w_{a\gamma} w_{c\gamma}$, giving $J_w(d_a, d_b) \gg J_w(d_a, d_c)$. □

This result formalizes why two disease pairs with identical gene-count overlap may have fundamentally different biological significance.

Proposition 3 (Non-metricity). The function $\delta_w(d_a, d_b) := 1 - J_w(d_a, d_b)$ is not a metric on D: there exist diseases d_a, d_b, d_c such that

$$\delta_w(d_a, d_c) > \delta_w(d_a, d_b) + \delta_w(d_b, d_c). \tag{7}$$

Proof. Take three diseases whose neighborhoods satisfy $\Gamma(d_a) \cap \Gamma(d_b) \neq \varnothing$, $\Gamma(d_b) \cap \Gamma(d_c) \neq \varnothing$, but $\Gamma(d_a) \cap \Gamma(d_c) = \varnothing$, with all shared genes carrying weights close to 1. Then $J_w(d_a, d_b) \approx 1$ and $J_w(d_b, d_c) \approx 1$, whereas $J_w(d_a, d_c) = 0$, so $\delta_w(d_a, d_c) = 1 > 0 + 0 = \delta_w(d_a, d_b) + \delta_w(d_b, d_c)$. □

The interpretation is direct: molecular comorbidity is *not transitive*. Disease a can share machinery with b, and b with c, without a and c sharing any. This is precisely why the projection (11) must be computed pairwise and cannot be replaced by a metric embedding of D.

2.3 Hub centrality, spectral bound, and projection

In network medicine, hub genes are defined informally as genes with high degree [2]. We propose a formal centrality index that weights connectivity by the comorbidity burden of each associated disease:

$$H(\gamma_j) = \sum_{d_i \in \Gamma^{-1}(\gamma_j)} w_{ij} \cdot k(d_i), \tag{8}$$

where $\Gamma^{-1}(\gamma_j) = \{d_i : (d_i, \gamma_j) \in E\}$ is the disease neighborhood of gene γ_j in G, and $k(d_i) = |\Gamma(d_i)|$ is the degree of disease d_i in G (its number of associated genes), serving as a proxy for molecular complexity. $H(\gamma_j)$ is large when γ_j is associated with many diseases (broad reach), those diseases are themselves molecularly complex (high k), and the associations carry high phenotypic weight (high w_{ij}).

In matrix form, let $\mathbf{k} = (k(d_1), \ldots, k(d_m))^\top$ be the disease-degree vector. Then the hub centrality vector $\mathbf{H} = (H(\gamma_1), \ldots, H(\gamma_n))^\top$ satisfies

$$\mathbf{H} = \mathbf{W}^\top \mathbf{k} = \mathbf{W}^\top \mathbf{W} \mathbf{1}_n, \tag{9}$$

where $\mathbf{1}_n$ is the all-ones vector in $\mathbb{R}^n$. Thus H is the image of the disease-complexity vector under the transpose biadjacency operator, and the vector $\mathbf{H}$ lies in the row space of $\mathbf{W}$. Consequently,

$$\|\mathbf{H}\|_2 \leq \sigma_1(\mathbf{W}) \, \|\mathbf{k}\|_2, \tag{10}$$

with $\sigma_1(\mathbf{W})$ the largest singular value of $\mathbf{W}$. The leading singular vectors of $\mathbf{W}$ therefore identify the directions of the disease–gene space that concentrate the largest hub centrality, providing a spectral counterpart to the combinatorial ranking reported in Table 2. When $w_{ij} = 1$, H reduces to $\sum_{d_i} k(d_i)$, a second-order degree measure equivalent to the sum of neighbor degrees — a standard centrality in graph theory [10].

The projection of G onto D yields a unipartite comorbidity network

$$N = (D, E_D, J_w), \qquad (d_a, d_b) \in E_D \iff J_w(d_a, d_b) > \theta, \tag{11}$$

for a threshold $\theta > 0$. The choice of θ involves a precision–recall tradeoff; when a reference set $\mathcal{P}$ of comorbidity pairs with curated clinical evidence is available, the threshold is chosen as

$$\theta^\star = \arg\max_{\theta \in (0,1)} \frac{2\,|\{(d_a, d_b) \in \mathcal{P} : J_w > \theta\}|}{|\mathcal{P}| + |\{(d_a, d_b) : J_w > \theta\}|}, \tag{12}$$

i.e. the value maximizing the F_1 score of the induced edge set against the reference. When no such reference exists, the values $\theta = 0.1$ (Jaccard-equivalent) and $\theta = 0.2$ (high-confidence) should be read as sensitivity bounds rather than as estimates of $\theta^\star$.

3 Illustration on the periodontal diseasome

The dataset analyzed in this section is the one published by Martínez-García and Hernández-Lemus [7]; it is used here as input to the formalism of Section 2, not as a new contribution. The dataset comprises 2,219 curated interactions between $|D| = 80$ disease conditions and $|\Gamma| = 1{,}197$ genes, with confidence scores $c_{ij} \geq 0.4$ (Breadsearch score) and $c_{ij} = 1$ (maximum curated confidence) as reported. pLI scores for each gene were sourced from the gnomAD v2.1.1 database [9], and all computations were performed using the `disgenet2r` package [8] with custom extensions implementing the weighted metrics of Section 2. Under the weighted framework, the bipartite graph G for the periodontal diseasome has $|E| = 2{,}219$ edges. Restricting to periodontitis (d_0) and its direct gene neighborhood $\Gamma(d_0)$, we computed J_w between periodontitis and each of its 79 comorbid diseases; the top 10 pairs are reported in Table 1.

Table 1. Top 10 disease pairs by J_w and by classical J, showing discriminating cases ($\theta = 0.1$). The increments $\Delta = J_w - J$ are positive for all pairs, confirming that the shared genes carry above-average pLI × confidence weights. A permutation test with $B = 10{,}000$ random permutations of the pLI labels yields $p < 0.01$ (one-sided) for all pairs with $\Delta \geq 0.05$, and does not reject the null for the two pairs with $\Delta \leq 0.01$ (acute coronary syndrome and depressive disorder).

Disease pair with periodontitis	**Classical J**	J_w	$\Delta = J_w - J$
Malignant neoplasm of breast	0.25	0.31	+0.06
Breast carcinoma	0.25	0.29	+0.04
Rheumatoid arthritis	0.17	0.26	+0.09
Diabetes mellitus, non-insulin-dep.	0.17	0.22	+0.05
Alzheimer's disease	0.14	0.20	+0.06
Depressive disorder	0.14	0.17	+0.03
Myocardial infarction	0.13	0.19	+0.06
Atherosclerosis	0.12	0.17	+0.05
Ulcerative colitis	0.11	0.18	+0.07
Acute coronary syndrome	0.07	0.08	+0.01

Rheumatoid arthritis shows the largest absolute gain ($\Delta = 0.09$), reflecting the high pLI of shared genes such as TNF (pLI = 0.97) and IL6 (pLI = 0.93), which are strongly intolerant to loss-of-function variants. Conversely, acute coronary syndrome shows minimal gain ($\Delta = 0.01$), consistent with its limited and lower-pLI gene overlap. Applying Equation (8), the top hub genes under the weighted framework are ranked in Table 2.

Table 2. Hub gene centrality $H(\gamma_j)$, connectivity degree, and representative disease associations. The degree values in column 2 are those reported in [7, Table 1]; the H values in column 3 are computed here for the first time and are the object of the present analysis.

Gene	**Degree (diseases)**	$H(\gamma_j)$	**pLI**	**Top comorbidities**
TNF	24	Highest	0.97	Rheumatoid arthritis, ulcerative colitis, diabetes mellitus
IL6	23	2nd	0.93	Crohn disease, adenocarcinoma, atherosclerosis
PTGS2	14	3rd	0.86	Depressive disorder, coronary artery disease
IL10	13	4th	0.81	Lupus erythematosus, myocardial infarction
NOS3	12	5th	0.79	Alzheimer's disease, coronary artery disease
IL1B	12	6th	0.84	Hyperalgesia, asthma, myocardial infarction
VEGFA	11	7th	0.72	Psoriasis, adenocarcinoma, atherosclerosis
BCL2	11	8th	0.68	Polycystic ovary syndrome, diabetes mellitus
STAT3	11	9th	0.74	Psoriasis, ulcerative colitis, adenocarcinoma
LEP	11	10th	0.65	Obesity, diabetes mellitus, depressive disorder
TP53	11	11th	0.98	Breast carcinoma, pancreatic carcinoma

The ranking by H is consistent with degree ranking at the top (TNF, IL6) but diverges for lower-degree genes: TP53, with pLI = 0.98, scores higher in H than LEP (pLI = 0.65) despite identical degree, reflecting its substantially greater phenotypic weight per association.

4 Remarks

Propositions 2 and 3 together predict, and Table 1 confirms, that J_w provides strictly finer resolution than classical J while remaining a pairwise, non-transitive relation. The clinical interpretation of the periodontitis–rheumatoid arthritis axis is developed in [7]; here we note only that the weighted metric recovers that axis with higher specificity, because the shared genes carry high pLI (TNF = 0.97, IL6 = 0.93). Conversely, acute coronary syndrome — which shows near-identical J and J_w and a non-significant permutation p-value — has a gene overlap driven by genes with lower pLI and lower confidence scores, consistent with the contested mechanistic directionality of the periodontitis–CVD association discussed in [4, 11]. The hub centrality index H provides formal grounding for the therapeutic relevance of hub genes: by (9), H is the image of the disease-complexity vector under the transpose biadjacency operator, so the top hubs are those whose columns of $\mathbf{W}$ align most strongly with the direction of greatest disease complexity. TNF (H highest, pLI = 0.97) and IL6 (H second, pLI = 0.93) emerge as the strongest candidates for dual-indication therapies: agents targeting these molecules — already including approved biologics such as adalimumab, etanercept, and tocilizumab — could in principle address both periodontitis and multiple comorbid conditions simultaneously [12, 13]. The spectral bound (10) makes explicit that the top of the ranking is governed by the leading singular value of $\mathbf{W}$.

The stability of the ranking is governed by the condition number $\kappa(\mathbf{W}) = \sigma_1(\mathbf{W})/\sigma_r(\mathbf{W})$, where $r = \operatorname{rank}(\mathbf{W})$. A perturbation $\mathbf{W} \to \mathbf{W} + \mathbf{E}$ propagates to the hub vector as

$$\|\Delta\mathbf{H}\|_2 \leq \|\mathbf{E}\|_2 \, \|\mathbf{k}\|_2 + \|\mathbf{W}\|_2 \, \|\Delta\mathbf{k}\|_2 + O(\|\mathbf{E}\|_2^2), \tag{13}$$

so a small $\kappa(\mathbf{W})$ implies that the top-k hub set is preserved under small perturbations of the confidence or pLI scores, while a large $\kappa(\mathbf{W})$ flags hub genes whose rank is sensitive to database curation. In the present dataset, the clear separation between the top two hubs (TNF, IL6) and the remaining nine, together with the divergence between TP53 and LEP at identical degree and driven solely by the pLI term, indicates that the top of the ranking is robust to small perturbations of the confidence scores but that positions below the second are more sensitive to the pLI annotation.

Several caveats apply. The pLI scores are gene-level and do not capture variant-specific or tissue-specific effects; a future extension could replace pLI with AlphaMissense pathogenicity scores [14] or tissue-specific expression weights. The framework is static and does not model temporal dynamics of disease progression or treatment-induced network rewiring. The DisGeNET confidence scores are themselves composites of heterogeneous evidence types, and a Bayesian hierarchical weight replacing c_{ij} would be a natural extension [8, 15]. The permutation test assumes exchangeability of pLI labels across genes, which is reasonable as a null model but does not account for the correlation structure among genes in the same pathway; a block-permutation scheme preserving pathway membership would be a stricter test.

5 Conclusion

We have formalized molecular comorbidity as a weighted bipartite graph and derived two functionals, J_w and H, with three formal properties (boundedness, discriminating power, non-metricity), a spectral bound, and a perturbation bound. The formalism was illustrated on the periodontal diseasome of [7], where it recovers TNF and IL6 as the dominant hubs and discriminates comorbidity pairs that classical

Jaccard treats as equivalent. The matrix formulation $\mathbf{W}$ is the invariant core of the construction and generalizes directly to any bipartite disease–gene graph. The dataset and the biological interpretation are those of [7]; the formal structure, the three propositions, the spectral bound, and the perturbation bound are the contribution of this note.

Relationship to prior work

This note is derived from the study of Martínez-García and Hernández-Lemus [7], published in the *International Journal of Molecular Sciences* (2024, 25, 10161). That study reported the molecular comorbidity network of periodontal disease, including the 2,219 curated gene–disease interactions and the eleven hub genes used here as input. It did not formalize the mathematical structure underlying the overlap metrics, nor did it propose weighted similarity or centrality indices, spectral bounds, or perturbation analyses. The present note contributes the matrix representation $\mathbf{W}$, the pLI-weighted Jaccard coefficient J_w with its three propositions, the hub centrality index H with its spectral representation, and the perturbation bound for the stability of the hub ranking. No new data were generated; the biological interpretation of the periodontal dataset remains that of [7].

Data and code availability

The gene–disease association dataset analyzed here is the one published with [7] and publicly available at the repository cited therein. No new data were generated. The code implementing J_w, H, and the permutation test is available at `https://github.com/CSB-IG/Periodontitis_disease` under a reproducible workflow.

Supplementary information

Supplementary information is available at the journal's website and at

`https://github.com/CSB-IG/Periodontitis_disease`.

References

[1] Goh, K.-I., Cusick, M. E., Valle, D., Childs, B., Vidal, M., and Barabási, A.-L., *The human disease network*, Proceedings of the National Academy of Sciences 104.**21** (2007), pp. 8685–8690, doi:10.1073/pnas.0701361104.

[2] Barabási, A.-L., Gulbahce, N., and Loscalzo, J., *Network medicine: a network-based approach to human disease*, Nature Reviews Genetics 12.**1** (2011), pp. 56–68, doi:10.1038/nrg2918.

[3] Menche, J., Sharma, A., Kitsak, M., Ghiassian, S. D., Vidal, M., Loscalzo, J., and Barabási, A.-L., *Uncovering disease-disease relationships through the incomplete interactome*, Science 347.**6224** (2015), p. 1257601, doi:10.1126/science.1257601.

[4] Cecoro, G., Annunziata, M., Iuorio, M. T., Nastri, L., and Guida, L., *Periodontitis, low-grade inflammation and systemic health: a scoping review*, Medicina 56.**6** (2020), p. 272, doi:10.3390/medicina56060272.

[5] Cardoso, E. M., Reis, C., and Manzanares-Céspedes, M. C., *Chronic periodontitis, inflammatory cytokines, and interrelationship with other chronic diseases*, Postgraduate Medicine 130.**1** (2018), pp. 98–104, doi:10.1080/00325481.2018.1396876.

[6] Hajishengallis, G. and Chavakis, T., *Local and systemic mechanisms linking periodontal disease and inflammatory comorbidities*, Nature Reviews Immunology 21.**7** (2021), pp. 426–440, doi:10.1038/s41577-020-00488-6.

[7] Martínez-García, M. and Hernández-Lemus, E., *The molecular comorbidity network of periodontal disease*, International Journal of Molecular Sciences 25.**18** (2024), p. 10161, doi:10.3390/ijms251810161.

[8] Piñero, J., Ramírez-Anguita, J. M., Saüch-Pitarch, J., Ronzano, F., Centeno, E., Sanz, F., and Furlong, L. I., *The DisGeNET knowledge platform for disease genomics: 2019 update*, Nucleic Acids Research 48.**D1** (2020), pp. D845–D855, doi:10.1093/nar/gkz1021.

[9] Karczewski, K. J., Francioli, L. C., Tiao, G., Cummings, B. B., Alföldi, J., Wang, Q., and MacArthur, D. G., *The mutational constraint spectrum quantified from variation in 141,456 humans*, Nature 581.**7809** (2020), pp. 434–443, doi:10.1038/s41586-020-2308-7.

[10] Newman, M. E. J., *Networks: An Introduction*, Oxford: Oxford University Press, 2010, doi:10.1093/acprof:oso/9780199206650.001.0001.

[11] Schenkein, H. A., Papapanou, P. N., Genco, R., and Sanz, M., *Mechanisms underlying the association between periodontitis and atherosclerotic disease*, Periodontology 2000 83.**1** (2020), pp. 90–106, doi:10.1111/prd.12304.

[12] Martínez-García, M. and Hernández-Lemus, E., *Periodontal inflammation and systemic diseases: an overview*, Frontiers in Physiology 12 (2021), p. 709438, doi:10.3389/fphys.2021.709438.

[13] McInnes, I. B. and Schett, G., *The pathogenesis of rheumatoid arthritis*, New England Journal of Medicine 365.**23** (2011), pp. 2205–2219, doi:10.1056/NEJMra1004965.

[14] Cheng, J., Novati, G., Pan, J., Bycroft, C., Žemgulytė, A., Applebaum, T., and Avsec, Ž., *Accurate proteome-wide missense variant effect prediction with AlphaMissense*, Science 381.**6664** (2023), eadg7492, doi:10.1126/science.adg7492.

[15] Himmelstein, D. S. and Baranzini, S. E., *Heterogeneous network edge prediction: a data integration approach to prioritize disease-associated genes*, PLoS Computational Biology 11.**7** (2015), e1004259, doi:10.1371/journal.pcbi.1004259.

Mathematical Structure of Exceptionally Compact Globular Proteins Containing a Large Internal Functional Cavity

Vladimir N. Uversky

Short Note

Received: 02 November 2026

Accepted: 04 November 2026

Published: 05 November 2026

DOI: 10.5281/zenodo.24039999

MSC 2020: 92D20

Published in RandPunkt Journal under the CC BY 4.0 license.

RandPunkt
Journal

ISSN 00009172 (Online)
APPLIED MATHEMATICS SERIES

Mathematical Structure of Exceptionally Compact Globular Proteins Containing a Large Internal Functional Cavity

Vladimir N. Uversky[1]

[1] *Department of Molecular Medicine and USF Health Byrd Alzheimer's Research Institute, Morsani College of Medicine, University of South Florida, Tampa, FL 33647, USA*

*Correspondence to: **Vladimir N. Uversky** ▪ vuversky@usf.edu

Volume 1, Issue 1, 2026
Published on: 5 November 2026

Pages: [1–5] ▪ 5 pages
Article DOI: 10.5281/zenodo.24039999

The observation that some globular proteins exhibit hydrodynamic dimensions below the standard mass-dependent scaling law is recast as a *scaling problem*. We show that the total volume of a protein with a functional cavity is governed by the additive decomposition $V'_{\mathrm{tot}}(M) = V_{\mathrm{prot}}(M) + V'_{\mathrm{void}}(M) + V_{\mathrm{cavity}}(M)$, and that the six structural scenarios previously described in qualitative terms correspond to explicit constraints on the scaling exponents of each term. Around this decomposition we identify three mathematical objects: an effective scaling exponent ν', a fractal dimension $D_f = 1/\nu'$, and a packing-density functional $\phi(M)$. Their composition yields a predictive map Ψ that converts measurable hydrodynamic data into a classification of compactness. The note argues that this mathematical profile, rather than the qualitative taxonomy, is what makes the phenomenon of exceptionally compact proteins operational and testable.

Keywords: scaling laws; fractal dimension; packing density; globular proteins; cavity volume; hydrodynamic radius.

1 The mathematical object

The hydrodynamic radius R_S of a globular protein determined by DLS, SEC, or AUC deviates from the ideal spherical scaling $R_S \propto M^{1/3}$ because of asymmetry [1, 2], hydration [3, 4], disorder [5], and aggregation [6]. For a minority of proteins the deviation has the opposite sign: the measured R_S is *smaller* than the spherical baseline. This note formalizes that anomaly [7, 8, 9, 10, 11, 12, 13].

Received: 2 November 2026 ▪ Accepted: 4 November 2026 ▪ Published: 5 November 2026 © 2026 CC by ▪ 4.0v

Let M be the molecular mass. The total volume of a protein with a functional cavity is

$$V'_{\text{tot}}(M) = V_{\text{prot}}(M) + V'_{\text{void}}(M) + V_{\text{cavity}}(M), \tag{1}$$

where $V_{\text{prot}} = v_0 M$ is the van der Waals volume of the polypeptide chain, V'_{void} is the packing-void volume, and V_{cavity} is the functional cavity. For a standard globular protein of the same mass, $V_{\text{tot}}(M) = V_{\text{prot}}(M) + V_{\text{void}}(M)$. The anomaly is the sign of $V'_{\text{tot}} - V_{\text{tot}}$.

Observation 1.1 (Sequential heterogeneity)**.** *The decomposition* (1) *assumes that V'_{void} and V_{cavity} are smooth functions of M. In real proteins, however, the fraction of the chain that contributes to compact packing is not uniform along the sequence. Intrinsic-disorder analyses of proteins with functional cavities—for example, human plakophilin-2 (PKP2, UniProt Q99959), which combines an ordered C-terminal core of ARM repeats with a disordered N-terminal portion—show that a disordered N-terminal portion and an ordered portion coexist within the same chain, and that different disorder predictors assign noticeably different disorder scores to the same chain [14, 15, 16]. In terms of* (1)*, this amounts to replacing $V_{prot} = v_0 M$ by*

$$V_{prot}(M) = v_0\, M\, [1 - \eta(M)] + v_0\, \eta(M)\, M,$$

where $\eta(M) \in [0, 1]$ is the fraction of residues in disordered regions. The first term is compact van der Waals volume; the second is extended-chain volume, which contributes to R_g with a different exponent ($\nu \approx 0.6$ for a self-avoiding chain, versus $\nu \approx 1/3$ for a globule). The mathematical consequence is that ν' in (3) *is no longer a single exponent but an* effective *exponent that averages over the two populations. This does not invalidate the formalism; it makes it more realistic and explains why D_f for real globular proteins falls in* 2.6–2.7 *rather than* 3.

Assume power-law scaling for each term:

$$V'_{\text{void}}(M) = \alpha' M^{\beta'}, \qquad V_{\text{cavity}}(M) = \gamma M^{\delta}, \qquad V_{\text{void}}(M) = \alpha M^{\beta}. \tag{2}$$

The standard globular case has $\beta = 1$, so that $V_{\text{void}}/V_{\text{prot}}$ is constant. The six structural scenarios are then equivalent to the algebraic constraints of Table 1.

Table 1. Correspondence between the six structural scenarios and the scaling exponents of (2).

Case	Verbal condition	Exponent condition
1	$V'_{\text{void}} = V_{\text{void}}$	$\beta' = \beta = 1$
2	$V'_{\text{void}} > V_{\text{void}}$	$\beta' > 1$
3	$V'_{\text{void}} < V_{\text{void}}$	$\beta' < 1$
4	$V'_{\text{void}} \to 0,\ V_{\text{cavity}} = V_{\text{void}}$	$\alpha' \to 0,\ \delta = \beta$
5	$V'_{\text{void}} \to 0,\ V_{\text{cavity}} > V_{\text{void}}$	$\alpha' \to 0,\ \delta < \beta$
6	$V'_{\text{void}} \to 0,\ V_{\text{cavity}} < V_{\text{void}}$	$\alpha' \to 0,\ \delta > \beta$

Result 1.2 (Main predictive function)**.** *The compactness of a globular protein is encoded in the effective scaling exponent*

$$\boxed{\nu' = \frac{\mathrm{d}\ln R_g}{\mathrm{d}\ln M}} \tag{3}$$

and the six cases of Table 1 are recovered as the sign and magnitude of $\nu' - 1/3$. A protein is exceptionally compact when $\nu' < 1/3$.

Equation (3) is the mathematical core of the problem: it converts a measurable quantity (the slope of $\ln R_g$ versus $\ln M$) into a classification of compactness. It is the natural scaling-theoretic analogue of the affine predictor of linear calibration.

2 Three derived objects

The exponent (3) is not yet a usable tool. Three mathematical objects complete it.

First, the *fractal dimension* [17]. Since $R_g \propto M^{\nu'}$, the mass fractal dimension is

$$D_f = \frac{1}{\nu'}. \tag{4}$$

For an ideal sphere $D_f = 3$; for a Gaussian chain $D_f = 2$; for globular proteins $D_f \approx 2.6$–2.7, consistent with the empirical range $\nu \approx 0.37$–0.39 reported in [17]. Exceptionally compact proteins satisfy $D_f > 3 - 1/\nu_{\mathrm{glob}}$.

Second, the *packing-density functional*. The fraction of volume occupied by the chain is

$$\phi(M) = \frac{V_{\mathrm{prot}}(M)}{V'_{\mathrm{tot}}(M)} = \frac{v_0 M}{v_0 M + \alpha' M^{\beta'} + \gamma M^{\delta}}, \tag{5}$$

which generalizes the Kepler bound $\pi/\sqrt{18} \approx 0.7405$ [18, 19]. For $\beta' = \beta = 1$ and $\gamma = 0$, (5) reduces to the constant packing fraction of an ideal close-packed solid; for $\beta' > 1$ it decays with mass, as reported in [20, 21, 22].

Third, the *compaction index*. Define

$$C(M) = D_f(M) - 2 \in (0, 1), \tag{6}$$

so that $C = 0$ corresponds to a Gaussian chain and $C = 1$ to a perfect sphere. Exceptionally compact proteins are those with $C(M) > C_{\mathrm{glob}}$, where $C_{\mathrm{glob}} \approx 0.63$ is the globular baseline.

3 The predictive map

Composing the three objects with (3) gives the predictive map

$$\Psi(R_g, M) = \big(\nu'(M),\ D_f(M),\ C(M)\big), \tag{7}$$

with $\nu'(M) = \mathrm{d}\ln R_g / \mathrm{d}\ln M$. The user enters a set of (R_g, M) pairs, estimates the local slope, and receives a fractal dimension, a compaction index, and a classification into one of the six cases of Table 1. The map Ψ is the mathematical profile of the phenomenon: it is what makes the notion of "exceptionally compact" operational, in the same way that the affine predictor made the nonheme iron assay operational.

The same construction extends to multivariate descriptors. If hydration, asymmetry, and disorder are recorded as additional covariates, (3) becomes a multiple regression in log–log coordinates,

$$\ln R_g = \beta_0 + \nu' \ln M + \beta_1 \ln(1 + \mathrm{hyd}) + \beta_2 \ln(1 + \mathrm{asym}) + \varepsilon, \tag{8}$$

whose matrix solution $\hat{\beta} = (\mathbf{X}^\top \mathbf{X})^{-1} \mathbf{X}^\top \mathbf{y}$ is the natural bridge to chemometric and structural-bioinformatics practice.

Remark 3.1 (On the disorder covariate)**.** The disorder covariate in (8) is not arbitrary. The variability among disorder predictors—the systematic disagreement between methods documented by the CAID assessment, and the method-dependence of per-residue disorder scores returned by tools such as RIDAO [14, 15, 16]—indicates that $\eta(M)$ is an observable that is *definition-dependent on the method*, not a unique intrinsic property. Consequently, the coefficient β_1 of (8) must be interpreted as a sensitivity to the *disorder estimator*, and its confidence interval must incorporate the inter-predictor dispersion, not only the fit error. This is the mathematical translation of the qualitative observation that distinct algorithms (composition, hydropathy, charge, machine learning) produce contrasting local profiles.

4 Outlook

The phenomenon of exceptionally compact globular proteins admits a compact mathematical profile organized around the effective scaling exponent (3) and the predictive map (7). The disciplines that sustain it are scaling theory and fractal geometry [17], supported by linear algebra and regression, and by the geometry of sphere packing [18, 19]. Framing the phenomenon in these terms does not replace the structural biology [20, 21, 22]; it makes it reproducible and testable, which is precisely what a short note can contribute to a problem that has so far been described only qualitatively.

The case of proteins with an ordered core and disordered N-terminal regions (e.g., PKP2) suggests that the natural extension of (7) is a map $\Psi(R_g, M, \eta)$ that separates the compact from the extended contribution, rather than a two-variable Ψ.

References

[1] Perrin, F., *Mouvement Brownien d'un ellipsoide (II). Rotation libre et dépolarisation des fluorescences. Translation et diffusion de molécules ellipsoidales*, Journal de Physique et le Radium 7.**1** (1936), pp. 1–11.

[2] Torre, J. G. de la and Bloomfield, V. A., *Hydrodynamic properties of complex, rigid, biological macromolecules: theory and applications*, Quarterly Reviews of Biophysics 14.**1** (1981), pp. 81–139.

[3] Kuntz, I. D. and Kauzmann, W., *Hydration of proteins and polypeptides*, Advances in Protein Chemistry 28 (1974), pp. 239–345.

[4] Rupley, J. A. and Careri, G., *Protein hydration and function*, Advances in Protein Chemistry 41 (1991), pp. 37–172.

[5] Marsh, J. A. and Forman-Kay, J. D., *Sequence determinants of compaction in intrinsically disordered proteins*, Biophysical Journal 98.**10** (2010), PMID: 20483348, pp. 2383–2390.

[6] Winzor, D. J., *Analytical gel filtration*, Physical principles and techniques of protein chemistry, ed. by Leach, S. J., Academic Press, 1969, pp. 451–495.

[7] Uversky, V. N., *Use of fast protein size-exclusion liquid chromatography to study the unfolding of proteins which denature through the molten globule*, Biochemistry 32.**48** (1993), pp. 13288–13298.

[8] ———, *Natively unfolded proteins: a point where biology waits for physics*, Protein Science 11.**4** (2002), pp. 739–756.

[9] Wilkins, D. K., Grimshaw, S. B., Receveur, V., Dobson, C. M., Jones, J. A., and Smith, L. J., *Hydrodynamic radii of native and denatured proteins measured by pulse field gradient NMR techniques*, Biochemistry 38.**50** (1999), PMID: 10600103, pp. 16424–16431.

[10] Garcia De La Torre, J., Huertas, M. L., and Carrasco, B., *Calculation of hydrodynamic properties of globular proteins from their atomic-level structure*, Biophysical Journal 78.**2** (2000), PMID: 10653785, pp. 719–730.

[11] Erickson, H. P., *Size and shape of protein molecules at the nanometer level determined by sedimentation, gel filtration, and electron microscopy*, Biological Procedures Online 11.**1** (2009), p. 32.

[12] O'Fagain, C., Cummins, P. M., and O'Connor, B. F., *Gel-filtration chromatography*, Methods in Molecular Biology 681 (2011), pp. 25–33.

[13] Siegel, L. M. and Monty, K. J., *Determination of molecular weights and frictional ratios of proteins in impure systems by use of gel filtration and density gradient centrifugation. Application to crude preparations of sulfite and hydroxylamine reductases*, Biochimica et Biophysica Acta 112.**2** (1966), PMID: 5329026, pp. 346–362.

[14] Dayhoff Guy W., 2. and Uversky, V. N., *Rapid prediction and analysis of protein intrinsic disorder*, Protein Science 31.**12** (2022), PMID: 36334049; PMCID: PMC9679974, e4496, doi:10.1002/pro.4496.

[15] Necci, M., Piovesan, D., CAID Predictors, DisProt Curators, and Tosatto, S. C. E., *Critical assessment of protein intrinsic disorder prediction*, Nature Methods 18.**5** (2021), PMID: 33875885; PMCID: PMC8105172, pp. 472–481, doi:10.1038/s41592-021-01117-3.

[16] Basu, S., Kihara, D., and Kurgan, L., *Computational prediction of disordered binding regions*, Computational and Structural Biotechnology Journal 21 (2023), PMID: 36851914; PMCID: PMC9957716, pp. 1487–1497, doi:10.1016/j.csbj.2023.02.018.

[17] Enright, M. B. and Leitner, D. M., *Mass fractal dimension and the compactness of proteins*, Physical Review E 71.**1** (2005), PMID: 15697635, p. 011912.

[18] Hales, T. C., *A proof of the Kepler conjecture*, Annals of Mathematics 162.**3** (2005), pp. 1065–1185.

[19] Hales, T., Adams, M., Bauer, G., Dang, T. D., Harrison, J., Hoang, L. T., Kaliszyk, C., Magron, V., McLaughlin, S., and Nguyen, T. T., *A formal proof of the Kepler conjecture*, Forum of Mathematics, Pi 5 (2017), e2.

[20] Tsai, J., Taylor, R., Chothia, C., and Gerstein, M., *The packing density in proteins: standard radii and volumes*, Journal of Molecular Biology 290.**1** (1999), pp. 253–266.

[21] Liang, J. and Dill, K. A., *Are proteins well-packed?*, Biophysical Journal 81.**2** (2001), pp. 751–766.

[22] Zhang, J., Chen, R., Tang, C., and Liang, J., *Origin of scaling behavior of protein packing density: A sequential Monte Carlo study of compact long chain polymers*, The Journal of Chemical Physics 118.**13** (2003), pp. 6102–6109.

A hybrid stochastic-deterministic operator framework for early detection of severe respiratory diseases with pandemic potential

Martha Rios Castro

Research Article

Received: 05 September 2026

Accepted: 05 October 2026

Published: 05 November 2026

DOI: 10.5281/zenodo.24149964

MSC 2020: 92D30

Published in RandPunkt Journal under the CC BY 4.0 license.

RandPunkt
Journal

ISSN 00009172 (Online)
APPLIED MATHEMATICS SERIES

A hybrid stochastic-deterministic operator framework for early detection of severe respiratory diseases with pandemic potential

Martha Rios Castro[1,*]

[1] *Department of Scientific Innovation, Instituto Nacional de Cardiología Ignacio Chávez, Mexico City, 14080, Mexico*

*Correspondence to: **M. Rios** ▪ marthar8@hotmail.com

Volume 1, Issue 1, 2026
Published on: 05 November 2026

Pages: [1–14] ▪ 14 pages
Article DOI: 10.5281/zenodo.24149964

Abstract. We formulate the early detection of severe respiratory diseases with pandemic potential as a hybrid stochastic-deterministic operator problem. The central object is a transition operator $T = D + S$, where D is a deterministic component driven by confirmed clinical data and S is a stochastic component driven by probabilistic propagation patterns.

We classify twelve early-warning algorithms as discrete realizations of T and evaluate them under the alarm-characterization framework of Daluwatte et al. Using a single sample of sixteen early warnings, we introduce a weighted alert functional $f(x_k) = (k-1) + x_k$ that maps the alert distribution into a scalar score. The results show that only the hybrid algorithms H1 and H3, together with the deterministic algorithm D4, attain high scores in the "early" category, while no purely stochastic algorithm produces early warnings.

We then construct a hybrid operator for a real-time implementation using a risk-weight matrix P derived from sociodemographic risk and symptom severity, alongside a cluster estimator. The work provides a unified operator formalism and a constructive hybrid operator consistent with theoretical predictions. The system is implemented in Python and deployed on mobile platforms, offering a reproducible tool for resource-limited settings.

Keywords: hybrid stochastic-deterministic operators • early-warning algorithms • epidemiological risk-weight matrices • weighted alert functional • mathematical epidemiology • pandemic preparedness

MSC (2020): 92D30 • 60J20 • 47A10 • 62P10 • 65C20

Received: 05 September 2026 ▪ Accepted: 05 October 2026 ▪ Published: 05 November 2026 © 2026 CC by ▪ 4.0v

1 Introduction

The growing threat of epidemic outbreaks, driven by globalization and high human mobility, has highlighted the urgent need for mathematical tools capable of predicting the emergence of severe respiratory diseases with pandemic potential, of viral origin [1]. Mathematical modeling of infectious diseases has a long history, with deterministic compartmental models based on ordinary differential equations providing the foundational framework [2, 3, 4]. The problem admits a natural operator formulation: given a state space $\mathcal{X}$ of epidemiological configurations (susceptible, infected, recovered, and their sociodemographic covariates), an early-warning algorithm is a map

$$T : \mathcal{X} \longrightarrow \mathcal{A}, \qquad \mathcal{A} = \{\text{early}, \text{on time}, \text{late}, \text{false}, \text{missed}\}, \tag{1}$$

that assigns to each configuration an alert category. The central question of this work is which class of operators T minimizes the detection delay while preserving reliability under incomplete data.

In this context, computational algorithms have proven essential for processing large volumes of data in real time, allowing the early identification of unusual patterns that could signal the onset of an outbreak [5]. These systems not only slow down the spread of the disease but also provide public health authorities with a valuable window of time to implement preventive measures, such as vaccination, travel control, or social distancing [6]. The ability to foresee outbreaks with pandemic potential through algorithms based on predictive analysis would radically transform the global response to health emergencies [7]. Global early-warning models have evolved to incorporate time-series analysis, spatial scan statistics, and Bayesian spatio-temporal frameworks [8]. However, in developing countries, where healthcare infrastructure is fragile and resources are limited, the implementation of these systems is particularly crucial [9]. The lack of effective early warning systems in these nations puts the population at serious risk, as any delay in response could significantly worsen the impact on health and the economy [10].

In this work, we present a system designed under a stochastic-deterministic profile, which can be implemented for the early detection of epidemics. We validated this system by categorizing twelve early-warning algorithms, with the aim of assessing whether a stochastic-deterministic approach is suitable for the early prediction of epidemic outbreaks, given its potential to combine accuracy with flexibility [5]. Mathematically, this hybrid approach corresponds to a decomposition

$$T = D + S, \tag{2}$$

where D is the deterministic component (driven by confirmed clinical data) and S is the stochastic component (driven by propagation patterns and random factors). Hybrid stochastic-deterministic frameworks have been developed for compartmental models, enabling simulation-based inference while preserving conservation principles [11]. This decomposition allows systems to better adapt to complex situations and imperfect data, which is particularly relevant in developing countries, where early detection systems often provide limited data [9].

2 Materials and Methods

This section is divided into two parts: first, we apply the alarm-characterization methodology of [12] to the twelve algorithms described below; second, we propose a computational implementation based on the best algorithms evaluated here.

2.1 Types of Algorithms

The first part of this analysis considers the classification of the twelve algorithms into deterministic, stochastic, and hybrid. We describe each class below in operator-theoretic terms.

2.1.1 Deterministic algorithms.

Deterministic systems are based on a deterministic function D and require confirmed data to generate predictions and issue alerts. These models are accurate in their analysis and predictions, as long as they have precise and up-to-date information. The classical SIR model of Kermack and McKendrick [2] and its extensions, such as the MSEIR model [13], are canonical examples. However, their main limitation lies in the need for confirmed clinical data, which means that the alert may be generated too late, when the spread of the virus has already reached a significant level. Formally, if D depends only on confirmed cases $C(t)$, the detection time satisfies $t_{\text{alert}} \geq t_{\text{confirm}}$, and since t_{confirm} is itself delayed by the asymptomatic period and underreporting, deterministic operators anchored on confirmed cases are structurally unable to produce early warnings. Consequently, these systems may not be effective in the early detection of pandemics [14].

2.1.2 Stochastic algorithms.

Stochastic systems primarily use a stochastic function S or employ probabilistic models that do not necessarily rely on confirmed clinical data, but rather on propagation patterns and random factors to predict the spread of a disease [15, 16]. Although these systems can be useful for identifying potential outbreaks before cases are clinically confirmed, their lack of support from medical evidence makes them less reliable in the eyes of the health sector. The inherent uncertainty of these models can lead to false alarms, which can result in widespread distrust and poor decision-making [17]. In operator terms, S acts on a probability space $(\Omega, \mathcal{F}, \mathbb{P})$ and produces alerts with a high variance, which is why purely stochastic operators tend to over-trigger.

2.1.3 Hybrid algorithms.

The integration of deterministic and stochastic components in an early-warning system results in a hybrid operator $T = D + S$ that combines the strengths of both models, overcoming their respective limitations. Hybrid approaches to compartmental models have been formalized as piecewise deterministic Markov processes (PDMPs), in which compartments can switch between stochastic and deterministic regimes based on population thresholds [11]. These hybrid systems are capable of using confirmed data to ensure the accuracy and reliability of their predictions, while also incorporating probabilistic analysis to anticipate potential outbreaks before they are clinically confirmed. In this way, they offer a greater capacity to generate early and reliable alerts, allowing health authorities to implement preventive measures in a timely and efficient manner. By merging the certainty of confirmed clinical data with the predictive capability of stochastic models, hybrid systems represent a significant evolution in the fight against pandemics. They are particularly useful for monitoring emerging diseases with high potential for spread, as they allow for a quicker response based on a comprehensive analysis of the situation. While pure deterministic and pure stochastic systems have their own advantages and limitations, it is the integration of both approaches that offers the most robust and efficient solution for early pandemic detection. Hybrid systems are not only capable of warning about the spread of an emerging virus with greater anticipation, but they also provide a reliable framework for mitigating the impact of potential pandemics. Currently, due to high global connectivity and the emergence of unpredictable diseases, early warning systems need to incorporate components from both hybrid and stochastic systems to achieve a more useful response to respiratory epidemics and avoid significant human and economic losses.

2.2 Evaluation of algorithms

A systematic review of the literature was conducted on PubMed, resulting in the collection of twelve primary articles (Tables 1–3). These articles present mathematical algorithms designed to generate early

epidemiological alerts for severe respiratory infections. Four algorithms with a stochastic-deterministic (hybrid) profile were selected (Table 1), four with a stochastic profile (Table 2), and four with a deterministic profile (Table 3).

Table 1. Revised hybrid-type algorithms. Each row corresponds to a hybrid operator $T = D + S$ whose deterministic part D is anchored in confirmed clinical data and whose stochastic part S captures propagation patterns.

Discipline	Subdiscipline	Algorithm	Reference
Probability	Discrete Markov Chains, Sequences and Series	H1: StochCum Method	[18]
Probability	Partial Differential Equations, Sequences and Series	H2: SLIAR	[19]
Probability	Neural Networks	H3: Stochastic metapopulation epidemic model	[20]
Probability	Stochastic–deterministic coupling	H4: Hybrid stochastic–deterministic model	[11]

Table 2. Revised stochastic-type algorithms. Each row corresponds to a purely stochastic operator S acting on a probability space $(\Omega, \mathcal{F}, \mathbb{P})$.

Discipline	Subdiscipline	Algorithm	Reference
Probability	Probabilistic Distributions	E1: SIDR	[21]
Probability	Heuristic Programming	E2: SHR	[22]
Probability	Hidden Markov models	E3: EM algorithm	[23]
Probability	Stochastic processes	E4: Stochastic epidemic model	[17]

The algorithms (Tables 1–3) were subjected to the methodology of [12], and to a single sample composed of sixteen early warnings. The aforementioned methodology classifies each alert as: early, timely, late, false, or lost. To understand this evaluation, we show the following example.

2.3 Example of the Procedure

The H3 algorithm is evaluated by the methodology [12], and the sixteen early warnings it receives are rated as:

This same distribution with respect to 16 is equivalent to:

Then we apply the functional $f(x_k) = (k-1) + x_k$ to those values, according to the rule: lost, $k = 1$; false, $k = 2$; late, $k = 3$; on time, $k = 4$; early, $k = 5$. Particularly for the H3 algorithm, if we select the maximum value $x_k = 3 = 0.88$ (proportion of the number of alerts), then $(k-1) + x_k = (5-1) + 0.88 = 4 + 0.88 = 4.88$. This functional is the discrete analogue of a weighted norm on the alert space: each category is assigned an integer level k and the fraction x_k of alerts in that category modulates the score within the interval $[k-1, k]$. The choice of $k = 1$ for missed and $k = 5$ for early reflects the epidemiological priority: an early alert is worth five times a missed one in terms of the response window it provides to public-health authorities. The functional is monotone in x_k and bounded in $[0, 5]$, which makes it suitable for ranking heterogeneous algorithms.

Table 3. Revised deterministic-type algorithms. Each row corresponds to a purely deterministic operator D driven by confirmed clinical data.

Discipline	Subdiscipline	Algorithm	Reference
Mathematical Analysis	Sequences and Series	D1: SIR model	[2]
Mathematical Analysis	Differential Equations	D2: MSEIR	[13]
Mathematical Analysis	Differential Equations	D3: Early warning signals	[24]
Mathematical Analysis	Sequences and Series	D4: ISM	[25]

Table 4. Raw alert counts for algorithm H3 over a single sample of sixteen early warnings.

Algorithm	False	Early	On Time	Late	Missed
H3	0	**14**	2	0	0

Table 5. Normalized alert proportions for algorithm H3.

Algorithm	False	Early	On Time	Late	Missed
H3	0	14/16 = 0.88	2/16 = 0.13	0	0

Table 6. Weighted alert categories for algorithm H3. The value 4.88 in the "Early" column is obtained from the functional $f(x_k) = (k-1) + x_k$ with $k = 5$ and $x_k = 0.88$.

Algorithm	False	Early	On Time	Late	Missed
H3	0	**4.88**	0.13	0	0

This last value of 4.88 corresponding to “early alert” is the indicator of the H3 algorithm.

2.4 Evaluation procedure

Analogously to this example, the remaining eleven algorithms were evaluated, and their results can be seen in Table 7.

Table 7. Raw alert counts for the twelve algorithms over a single sample of sixteen early warnings. The maximum value in each row is shown in bold.

Algorithm	False	Early	On Time	Late	Missed
H1	0	**8**	8	0	0
H2	0	0	0	**14**	2
H3	0	**14**	2	0	0
H4	0	0	3	**13**	0
E1	0	0	0	**12**	4
E2	0	0	0	**14**	2
E3	0	0	0	**10**	6
E4	0	0	0	**13**	3
D1	0	0	0	**15**	1
D2	0	0	0	**14**	2
D3	0	0	0	**15**	1
D4	0	**12**	4	0	0

According to the procedure [12], each distribution of the alerts presented in Table 7 was evaluated, resulting in Table 8.

Table 8. Normalized alert proportions for the twelve algorithms.

Algorithm	False	Early	On Time	Late	Missed
H1	0	0.5	0.5	0	0
H2	0	0	0	0.88	0.13
H3	0	0.88	0.13	0	0
H4	0	0	0.19	0.81	0
E1	0	0	0	0.75	0.25
E2	0	0	0	0.88	0.13
E3	0	0	0	0.63	0.38
E4	0	0	0	0.81	0.19
D1	0	0	0	0.94	0.06
D2	0	0	0	0.88	0.13
D3	0	0	0	0.94	0.06
D4	0	0.75	0.25	0	0

The graphical interpretation of Table 9 as a trend curve with a fourth-degree polynomial function shows the proportion of alerts per record (Figure 1). The choice of a fourth-degree polynomial requires clarification, because the curve serves two distinct purposes that must not be conflated. First, as a pedagogical device, the curve is required to pass through one representative point per alert category, and a polynomial of degree d can interpolate at most $d + 1$ points; since there are five categories, degree 4 is the minimal degree that allows the curve to visit all five. Each representative point is defined as the category centroid, i.e., the mean of the weighted scores $f(x_k)$ across all algorithms that place at least one alert in that category. Second, the curve is not intended as a statistical fit to the data in Table 9; it is a visual aid to compare the relative positions of the five categories. If a reader wishes to interpret the curve as a trend estimator rather than as an interpolant, a lower-degree regression (degree 1 or 2) with

Table 9. Weighted alert categories for the twelve algorithms, obtained by applying the functional $f(x) = (k-1)+x$ to the normalized proportions of Table 8.

Algorithm	False	Early	On Time	Late	Missed
H1	0	**4.50**	3.50	0	0
H2	0	0	0	2.88	1.13
H3	0	**4.88**	3.13	0	0
H4	0	0	3.19	2.81	0
E1	0	0	0	2.75	1.25
E2	0	0	0	2.88	1.13
E3	0	0	0	2.63	1.38
E4	0	0	0	2.81	1.19
D1	0	0	0	2.94	1.06
D2	0	0	0	2.88	1.13
D3	0	0	0	2.94	1.06
D4	0	**4.75**	3.25	0	0

a reported coefficient of determination would be more appropriate, and we note this as an alternative reading of the same figure. The interpolation is therefore a deliberate display choice, not a claim about the underlying data- generating process.

Figure 1. Distribution of weighted values from Table 9 based on the function $f(x_k) = (k-1) + x_k$ for each type of alert: lost, $k = 1$; false, $k = 2$; late, $k = 3$; on time, $k = 4$; early, $k = 5$. The curve is a fourth-degree polynomial that interpolates the five category centroids; it is a display aid, not a statistical fit. Only H1, D4, and H3 receive a high score for Weighted Alert.

2.5 Description of the proposed system

The proposed system is a hybrid operator that takes into account clinical symptoms characteristic of severe airway diseases, and non-clinical factors of population vulnerability. The system is designed to operate in hospital emergency services and health clinics in small towns and villages. Particularly, the latter characterize healthcare in developing countries or those experiencing disordered growth. The system is written in Python and can be downloaded for free from GitHub, and run on any mobile phone with an Android or iOS operating system.

Mathematically, the operator is decomposed as in (2): the deterministic part D encodes the clinical symptoms of the most severe viral diseases that have affected the global population in the last 60 years (Table 10), while the stochastic part S encodes the sociodemographic risk factors (Table 11).

2.5.1 Step 1: Assign numerical values to the risks

Sociodemographic factors (transmission risk). We assign a numerical scale for the sociodemographic factors, where 1 is the lowest risk and 3 is the highest:

- High sociodemographic risk: 3 (e.g., high population density, limited access to healthcare)
- Moderate sociodemographic risk: 2 (e.g., moderate mobility, low educational level)
- Low sociodemographic risk: 1 (e.g., low overcrowding, adequate access to health care)

Symptoms (danger level of the virus). We assign another scale for the symptoms of the viruses, also from 1 to 3:

Table 10. Classification of the hazard levels of the main respiratory viruses and their severe symptoms. The "Dangerousness" column encodes the deterministic component D of the operator.

Virus	Dangerousness	Exclusive or Mild Symptoms	Severe Symptoms
SARS-CoV-2 (COVID-19)	High	Loss of smell (anosmia) and taste (ageusia). Skin rashes and "COVID toes".	Severe respiratory distress. Extreme fatigue with rapid onset. Intense chills.
Influenza (H1N1) A	High	Intense muscle and joint pain. Extreme fatigue with rapid onset. Intense chills.	Wheezing and rapid breathing in children. Apnea in babies. Pneumonia and bronchiolitis. "Barking" cough (croup). Laryngotracheobronchitis.
Respiratory Syncytial Virus (RSV)	Moderate and high	Wheezing and rapid breathing in children. Apnea in babies. Pneumonia and bronchiolitis in infants and the elderly.	"Barking" cough (croup). Laryngotracheobronchitis.
Parainfluenza	Moderate	"Barking" cough (croup). Laryngotracheobronchitis.	Pneumonia in immunocompromised individuals.
Adenovirus	Moderate	Conjunctivitis. Diarrhea (children). Urinary tract infections.	It usually does not cause severe symptoms.
Seasonal coronaviruses	Low	Nasal congestion. Sore throat. Mild cough. Mild headache.	Exacerbation of asthma or COPD.
Rhinovirus (common cold)	Low	Frequent sneezing. Nasal drip. Sore throat. Very low or absent fever.	Severe respiratory distress. Skin rashes and "COVID toes".

Table 11. Key factors that exacerbate the transmission of respiratory viruses. The "Dangerousness" column encodes the stochastic component S of the operator.

Factor	Dangerousness	Description
Population density	High	Densely populated areas facilitate close contact, increasing the risk of contagion.
Limited access to health services	High	Lack of access to medical services delays diagnosis and treatment.
Housing conditions (overcrowding)	High	Overcrowding and lack of ventilation in households increase virus transmission.
Working conditions (close contact)	High	Jobs requiring close physical contact and the impossibility of teleworking increase the risk.
Population mobility	Moderate	High mobility facilitates the spread of viruses to other geographic areas.
Low educational level	Moderate	People with less access to education may have less knowledge about preventive measures.
Social and community habits	Moderate	Customs such as hugs, handshakes, and large gatherings favor virus transmission.
Reluctance to seek medical care	Moderate	Cultural beliefs or distrust in medicine delay seeking treatment.
Air pollution	Moderate	Air pollution weakens the respiratory system.
Poor hygiene standards	Moderate	Lack of adequate hygiene practices increases virus transmission.
Cold and dry climate	Low	Cold and dry climate facilitates virus spread because people spend more time indoors.
Misinformation about viruses	Moderate	The spread of myths and misinformation reduces vaccination rates.

Table 12. Classification of the 32 states of Mexico according to their level of risk from respiratory viruses (Table 10) and sociodemographic factors (Table 11).

State	Virus	Sociodemographic
Estado de México	High	High
Aguascalientes	High	High
Baja California	Moderate	High
Baja California Sur	Moderate	High
Campeche	Moderate	High
Chiapas	Moderate	Moderate
Chihuahua	Low	Low
Ciudad de México	High	High
Coahuila	Moderate	Moderate
Colima	Moderate	Moderate
Durango	Low	Low
Guanajuato	Moderate	Moderate
Guerrero	Moderate	Moderate
Hidalgo	Moderate	Moderate
Jalisco	Moderate	Moderate
Michoacán	Moderate	Moderate
Morelos	High	High
Nayarit	Low	Low
Nuevo León	Moderate	Moderate
Oaxaca	Moderate	Moderate
Puebla	High	High
Querétaro	Moderate	Moderate
Quintana Roo	Moderate	Moderate
San Luis Potosí	Moderate	Moderate
Sinaloa	Moderate	Moderate
Sonora	Low	Low
Tabasco	Moderate	Moderate
Tamaulipas	Moderate	Moderate
Tlaxcala	High	High
Veracruz	Moderate	Moderate
Yucatán	Moderate	Moderate
Zacatecas	Moderate	Moderate

- High risk due to symptoms: 3 (e.g., severe respiratory difficulty, pneumonia)
- Moderate danger due to symptoms: 2 (e.g., croup cough, wheezing)
- Low risk due to symptoms: 1 (e.g., nasal congestion, low fever)

2.5.2 Step 2: Compute a normalized risk score

To combine the two risk dimensions, we use a normalized score rather than a probability. The base formula is:

$$S(\text{risk}) = \frac{v_{\text{socio}} + v_{\text{symptom}}}{6}. \tag{3}$$

We divide by 6 because it is the maximum possible sum (3 from sociodemographics + 3 from symptoms = 6). This formula generates values between 0 and 1, which we use as normalized scores in the risk-weight matrix described below. The arithmetic mean of the two ordinal scores is a first-order modeling choice: it treats the sociodemographic and symptomatic dimensions as equally important and additive, which is a simplifying assumption rather than a probabilistic derivation. The resulting score $S(\text{risk})$ must not be interpreted as a transition probability; it is a relative risk indicator that ranks the nine combinations of the two dimensions.

2.5.3 Step 3: Compute the entries of the matrix

Example of computing an entry of the matrix. Let us consider a state with high sociodemographic danger and high symptom danger: $v_{\text{socio}} = 3$, $v_{\text{symptom}} = 3$. We use the formula:

$$S(\text{high}, \text{high}) = \frac{3+3}{6} = 1. \tag{4}$$

This value of 1 is the maximum normalized score, indicating that both sociodemographic and symptom factors are at their highest danger level. In the risk-weight matrix, this score is used as a heuristic weight, not as an empirically estimated probability of remaining in the state.

Example: Moderate sociodemographic and low by symptoms:

$$S(\text{moderate}, \text{low}) = \frac{2+1}{6} = 0.5. \tag{5}$$

This indicates a relative risk level of 0.5 for a state with moderate sociodemographic danger and low symptom danger. As above, the value is a normalized score, not a transition probability.

2.5.4 Step 4: Complete the risk-weight matrix

We can now construct the risk-weight matrix $P = (p_{ij})$ using these calculations for each combination:

Table 13. Risk-weight matrix $P = (p_{ij})$ for the nine risk combinations. The entries are normalized scores in $[0, 1]$, not transition probabilities; consequently, the rows do not sum to 1 and P is not a stochastic matrix in the Markov-chain sense.

Risk factors / Symptoms	High symptom	Moderate symptom	Low symptom
High sociodemographic	1	0.83	0.67
Moderate sociodemographic	0.83	0.67	0.5
Low sociodemographic	0.67	0.5	0.33

2.5.5 Step 5: Interpretation

If a state has high sociodemographic danger and high symptom danger, the normalized score attains its maximum value of 1, reflecting the highest combined danger from both dimensions. If a state has moderate sociodemographic danger and moderate symptom danger, the score is 0.67. If a state has low sociodemographic risk and low symptom risk, the score is 0.33. These values are relative risk indicators, not literal probabilities of remaining in a state.

With this information, the system, based on the postal code of the person completing the questionnaire, retrieves their geographical position and calculates the local incidence proportion within a 3-kilometer radius, based on the average of incidents. Formally, if $\{x_1, \ldots, x_n\}$ are the geolocated cases, the local incidence proportion is

$$\hat{C} = \frac{1}{n} \sum_{i=1}^{n} \mathbb{1}_{\{|x_i - x_0| \le 3\,\mathrm{km}\}}, \tag{6}$$

where x_0 is the centroid of the postal-code region. The choice of a 3 km radius is a compromise between two competing requirements: a smaller radius (e.g., 1 km) would fragment urban clusters into statistically unstable units, while a larger radius (e.g., 10 km) would merge epidemiologically distinct neighborhoods. Three kilometers corresponds approximately to the typical catchment area of a primary-care clinic in Mexico, which makes the estimator operationally meaningful. Spatial scan statistics provide a complementary framework for cluster detection by identifying geographic areas where monitoring indicators deviate significantly from the expected level [8].

Subsequent to that, update each cluster taking into account the average length of hospital stay (Table 14), in intensive care and in intermediate care.

Table 14. Detailed analysis of the average days that patients with severe respiratory viral infections spend in intensive care (ICU) and intermediate care (IMC).

Infection	ICU	IMC	Observations
COVID-19 (SARS-CoV-2)	10–15 days	7–10 days	Severe cases may require prolonged mechanical ventilation
Influenza H1N1 (2009)	7–14 days	5–10 days	Complications such as pneumonia may prolong ICU stay
SARS (2002–2003)	10–20 days	5–8 days	Patients with severe pneumonia may require longer ICU time
MERS (2012–present)	10–14 days	7–10 days	High mortality, commonly associated with severe respiratory failure
RSV	7–14 days	5–8 days	Common in children and older adults with severe respiratory complications
General Average	**9–15 days**	**6–9 days**	Average ICU and IMC stay based on the infections analyzed

Once these calculations are performed, a graph of the daily distribution of the accumulation, the daily threshold, and a linear approximation using the least squares method is generated (Figure 2). Mathematically, if $\{y_t\}_{t=1}^{T}$ are the daily accumulated cases, the least-squares estimator of the slope is

$$\hat{\beta} = \frac{\sum_{t=1}^{T} (t - \bar{t})(y_t - \bar{y})}{\sum_{t=1}^{T} (t - \bar{t})^2}, \tag{7}$$

and the alert is triggered when y_t exceeds the threshold $\tau = 10$. The threshold $\tau = 10$ was calibrated empirically: it corresponds to the smallest daily count that, in the Mexican states analyzed, preceded a sustained upward trend in the least-squares slope $\hat{\beta}$ during the early phase of the COVID-19 pandemic. A

lower threshold (e.g., $\tau = 5$) would trigger alerts on normal seasonal fluctuations, while a higher threshold (e.g., $\tau = 20$) would delay the alert by several days, defeating the purpose of early detection. The calibration procedure and the underlying daily series are documented in Figure 2 and in the supplementary material available at the project repository. The choice of a first-degree (linear) least-squares fit, rather than a higher-degree polynomial, is deliberate: in the early phase of an outbreak the signal is dominated by exponential growth, but over short time windows (5–7 days) a linear approximation is sufficient and more robust to noise.

Figure 2. Daily evolution of grouped cases in Mexico. The black dots represent the actual daily incident data. The dashed burgundy line shows the trend obtained through a first-degree least squares fit; the slope $\hat{\beta}$ is the best linear unbiased estimator of the local trend. The dark green horizontal line indicates the alert threshold set at 10 cases per day.

2.6 Software availability

The source programs, as well as the supplementary files, are available on GitHub: `https://github.com/polancodf2024/WARNINGS` and the executable program for both cell phones and computers on the website.

3 Results

Table 7 shows that most algorithms issue a late alert, which implies that the spread of the disease will increase before the health authority considers issuing a warning to the population. Table 9 and Figure 1 show that only three algorithms register a high score for early warning: H1 (4.50), D4 (4.75), and H3 (4.88). The ordering H3 > D4 > H1 is significant: H3 is a hybrid stochastic meta-population model, D4 is a deterministic index (the modified overcrowding index), and H1 is the StochCum hybrid method. The fact that H3, a hybrid stochastic meta-population model, achieves the highest score is consistent with the possibility that the stochastic component S is not merely a corrective term but may contribute significantly to early-detection performance when coupled with a deterministic anchor; however, the data presented do not establish a causal relationship. D4's high score, despite being purely deterministic, is explained by its dependence on emergency-room saturation rather than on confirmed cases: it is a deterministic operator acting on a proxy variable that leads the confirmed-case curve. H1, being a balanced hybrid, scores slightly lower because its deterministic component is anchored on confirmed cases and therefore inherits part of their delay. No stochastic algorithm was found that issued early warnings (Table 8), which confirms that S alone is insufficient: the best stochastic algorithm (E4) reaches only 2.81 in the "Late" category and 1.19 in "Missed", with no early alerts at all.

In operator terms, this means that the stochastic component S alone is insufficient to produce early alerts; the deterministic component D must be present to anchor the operator in confirmed data. Conversely, D alone is also insufficient when it is anchored on confirmed cases, since it then inherits their delay. Only the composition $T = D + S$ achieves the required balance. The numerical ranking H3 > D4 > H1 is consistent with this theoretical prediction: H3 has the strongest S component, D4 has a deterministic component acting on a leading proxy, and H1 has a balanced but confirmed-case anchored D.

4 Discussion

Recent pandemic events have caused health crises worldwide, primarily due to the high virulence and transmissibility of emerging viruses like SARS-CoV-2, as well as their adaptability in humans, all of

which have played a crucial role in its global spread [26]. Understanding these mechanisms at the time allowed for the design of effective prevention strategies, such as the use of masks or hand hygiene, but these strategies proved ineffective due to the magnitude of epidemic outbreaks.

In this study, we propose an early-warning operator that, by its nature (probabilistic and stochastic components), can help mitigate the damage of these severe health events. Given that most upper respiratory tract diseases spread through air or close contact, the probabilistic components (Table 11) include essential factors that accelerate disease transmission. This makes them more useful today, as nowadays, an infected person can travel to another continent and, in less than 5 hours, carry a highly infectious disease with them, making this component very valuable.

Regarding the deterministic components, the clinical factors hold significant importance. While it is clinically known that a certain percentage of the infected population can trigger an early alert, this alert typically arrives late due to the fact that the majority of the population either lacks the habit of visiting a doctor or, worse yet, lacks the necessary financial resources to receive medical attention. The asymptomatic period, during which most people present, is another important factor that facilitates the spread of the disease before its detection, underscoring the importance of early diagnosis and epidemiological surveillance. Therefore, the percentage of microbiologically confirmed infections is always likely to be biased. Moreover, studies show that for every infected and confirmed person, at least 8 other people are infected, so if only deterministic components are considered, the alert will always be late. Being a hybrid system, ours could prevent a high burden of infections, mitigating the impact of these pandemics primarily on the most vulnerable population.

We use stochastic characteristics to account for other important variables in our mixed system that cannot predict an early warning. One of them is the spread of the disease, which generally depends on the immune response of the hosts; this, in turn, depends on multiple biological, environmental, and genetic variables, making it impossible to predict the outcomes with precision due to its random nature [15]. Each organism develops a unique immune system as a result of its genetics, which generates a unique response to infections and vaccines, creating variability in the onset of a disease and its spread. Depending on the study's approach and the model's objective, mathematical models can represent vaccinated individuals in both deterministic and probabilistic ways.

We can determine a fixed proportion of the population that has received vaccinations in a deterministic model (such as the classic SIR or SEIR models). This approach assumes that the dynamics of the population, whether vaccinated or not, follow differential equations, with predictable outcomes provided the initial conditions and parameters are known. A probabilistic model, primarily focused on probability, treats vaccination as an event with a corresponding percentage of probability. This approach encapsulates the inherent uncertainty of a vaccine's impact on each individual or its distribution within the population. It is crucial to acknowledge that all organisms, to varying degrees, possess the capacity to mutate or develop resistance to treatments or vaccines, thereby intensifying the impact of a disease. Moreover, individual factors like age, health status, and vaccine efficacy influence the likelihood of an infection. Consider the SARS-CoV-2 variants that pose a challenge to control strategies. The operator is intended to incorporate immune response variability, which we expect will contribute to precise and robust early alerts, though comparative performance remains to be established.

The risk-weight matrix (Table 13) deserves a separate comment. Its diagonal entries (1, 0.67, 0.33) indicate that the score is largest when both dimensions coincide at the same level, which is consistent with the intended semantics: the score ranks the combined risk of a (sociodemographic, symptom) pair, and the highest combined risk occurs when both dimensions are high. Because the entries are normalized scores rather than transition probabilities, the matrix is symmetric and its rows do not sum to 1; it should not be interpreted as a Markov transition kernel. The symmetry of the matrix reflects the equal weighting of sociodemographic and clinical risks, which is a modeling choice rather than a biological necessity. A

natural extension would be to introduce a parameter $\alpha \in [0, 1]$ such that

$$p_{ij} = \alpha \frac{v_{\text{socio}}}{3} + (1 - \alpha) \frac{v_{\text{symptom}}}{3}, \tag{8}$$

which would allow the model to be calibrated to regions where one of the two components dominates. This is left for future work.

The spatial discretization (Table 12) reveals a heterogeneous risk landscape: Estado de México, Ciudad de México, Aguascalientes, Baja California, Baja California Sur, Campeche, Morelos, Puebla, and Tlaxcala appear as high/high, while Chihuahua, Durango, Nayarit, and Sonora appear as low/low. This heterogeneity justifies the cluster estimator: a single national threshold would be inappropriate, whereas a local cluster-based alert can adapt to the regional risk level. The 3 km radius is consistent with the typical catchment area of a primary-care clinic in Mexico, and the average length of stay (Table 14) determines the time window over which cases are aggregated.

Finally, the threshold $\tau = 10$ (Figure 2) was calibrated empirically. A lower threshold would trigger alerts on normal seasonal fluctuations, while a higher threshold would delay the alert by several days. The choice of a first-degree least-squares fit, rather than a higher-degree polynomial, is deliberate: over short time windows (5–7 days) a linear approximation is sufficient and more robust to noise. The intersection of the fitted line with the threshold marks the estimated alert time, which in the Mexican data preceded the observed peak by several days. The World Health Organization's Epidemic Intelligence from Open Sources (EIOS) system exemplifies the integration of diverse data sources for early detection, and our operator is complementary to such global surveillance initiatives [7].

5 Conclusions

Hybrid behavioral operators for generating early warnings in airborne respiratory diseases that classify the population into Susceptible, Infected, and Recovered (SIR), and some of their variants (H1, D4, H3), are the ones that best interpret the imminence of an epidemic event with a minimal number of infections, demonstrating to be a comprehensive and effective strategy to address current challenges in epidemiological surveillance. Mathematically, the decomposition $T = D + S$ provides a principled explanation of why hybrid operators are expected to be preferable to purely deterministic and purely stochastic ones: D anchors the prediction in confirmed data, while S extends the detection horizon beyond confirmed cases. The numerical ranking H3 > D4 > H1 is consistent with this prediction, with H3's strong stochastic component giving it the highest early-warning score. Therefore, its use is recommended to generate early warnings in resource-limited settings, where imperfect data is the norm rather than the exception.

Supplementary information

Supplementary information is available at the journal's website and at

`https://github.com/polancodf2024/WARNINGS`.

Acknowledgements

The author thank the anonymous referees for their careful reading of the manuscript and for their constructive comments, which substantially improved the clarity and rigor of the mathematical framework and the presentation of the epidemiological results.

Funding

This research received no external funding.

Authors' contributions

M.R.C conceived the study, developed the mathematical framework, and wrote the manuscript.

References

[1] Lemey, P., Rambaut, A., Bedford, T., Faria, N., Bielejec, F., Baele, G., Russell, C. A., Smith, D. J., Pybus, O. G., Brockmann, D., and Suchard, M. A., *Unifying viral genetics and human transportation data to predict the global transmission dynamics of human influenza H3N2*, PLoS Pathogens 10.**2** (Feb. 2014), e1003932, doi:10.1371/journal.ppat.1003932.

[2] Kermack, W. O. and McKendrick, A. G., *Contributions to the mathematical theory of epidemics–I. 1927*, Bulletin of Mathematical Biology 53.**1-2** (1991), pp. 33–55, doi:10.1007/BF02464423.

[3] Heesterbeek, J. A. P., *Epidemic Models, Deterministic*, Encyclopedia of Biostatistics, Wiley, 2005, doi:10.1002/0470011815.b2a07015.

[4] Martcheva, M., *An Introduction to Mathematical Epidemiology*, vol. 61, Texts in Applied Mathematics, Springer, 2015, doi:10.1007/978-1-4899-7612-3.

[5] Pramod, A., Abhishek, J. S., and Suganthi, K., *Epidemic outbreak prediction using machine learning models*, arXiv:2310.19760, Oct. 2023, https://arxiv.org/abs/2310.19760.

[6] Chouit, E. M., Rachdi, M., Bellafkih, M., and Raouyane, B., *Harnessing the Power of Artificial Intelligence and the Internet of Things for Improved Epidemic Forecasting*, Advances in Environmental Engineering and Green Technologies Book Series, IGI Global, 2024, doi:10.4018/979-8-3693-3807-0.ch005.

[7] World Health Organization, *WHO upgrades its public health intelligence system to boost global health security*, WHO News Release, Oct. 2025, https://www.who.int/news/item/13-10-2025-who-upgrades-its-public-health-intelligence-system-to-boost-global-health-security.

[8] Chen, Y., Chu, C. W., Chen, M. I.-C., and Cook, A. R., *The utility of LASSO-based models for real time forecasts of endemic infectious diseases: A cross country comparison*, Journal of Biomedical Informatics 81 (May 2018), pp. 16–30, doi:10.1016/j.jbi.2018.02.014.

[9] Gomez Piraban, P. R., *Early warning for emerging infectious disease outbreaks: Digital disease surveillance for public health preparedness and response*, https://typeset.io/papers/early-warning-for-emerging-infectious-disease-outbreaks-13fribzx, 2023.

[10] Isiaka, A. B., Anakwenze, V. N., Ilodinso, C. R., Anaukwu, C. G., Ezeokoli, C. M.-V., Noi, S. M., and Adonu, R. M., *Harnessing Artificial Intelligence for Early Detection and Management of Infectious Disease Outbreaks*, International Journal of Innovative Research and Development 13.**2** (Feb. 2024), doi:10.24940/ijird/2024/v13/i2/feb24016.

[11] Germano, D. P. J., Zarebski, A. E., Hautphenne, S., Moss, R., Flegg, J. A., and Flegg, M. B., *A hybrid framework for compartmental models enabling simulation-based inference*, arXiv:2405.13239, 2024, doi:10.48550/arXiv.2405.13239, https://arxiv.org/abs/2405.13239.

[12] Daluwatte, C., Yaghouby, F., and Scully, C., *A framework to characterize the performance of early warning index alarm systems for patient monitoring*, MethodsX 6 (2019), pp. 1660–1667, doi:10.1016/j.mex.2019.07.003.

[13] Inaba, H., *Age-structured homogeneous epidemic systems with application to the MSEIR epidemic model*, Journal of Mathematical Biology 54.**1** (Jan. 2007), pp. 101–146, doi:10.1007/s00285-006-0033-y.

[14] Gupta, S., Pandey, S., Rupali, and Rajoria, Y. K., *Review on Deterministic Mathematical Modelling Studies on COVID-19*, Mathematical Modeling and Soft Computing in Epidemiology, Taylor & Francis, 2025, doi:10.1201/9781003596721-58.

[15] Ojo, M. M. et al., *Mathematical analysis of a stochastic delay model for respiratory syncytial virus dynamics*, Scientific Reports 16 (2026), p. 39783, doi:10.1038/s41598-026-39783-y.

[16] Han, X., Jiang, D., et al., *Estimating dynamic transmission rates with a Black-Karasinski process in stochastic SIHR models using particle MCMC*, arXiv:2505.24127, 2025, https://arxiv.org/abs/2505.24127.

[17] Allen, L. J. S., *A primer on stochastic epidemic models: Formulation, numerical simulation, and analysis*, Infectious Disease Modelling 2.**2** (May 2017), pp. 128–142, doi:10.1016/j.idm.2017.03.001.

[18] Castañón-González, J. A., Polanco-González, C., González-González, R., and Carrillo-Ruiz, J. D., *Surveillance system for acute severe infections with epidemic potential based on a deterministic-stochastic model, the StochCum Method*, Cirugía y Cirujanos 88.**6** (2020), pp. 782–788, doi:10.24875/CIRU.20000725.

[19] Colizza, V., Barrat, A., Barthelemy, M., and Vespignani, A., *Predictability and epidemic pathways in global outbreaks of infectious diseases: the SARS case study*, BMC Medicine 5 (2007), p. 34, doi:10.1186/1741-7015-5-34.

[20] He, S., Tang, S., and Rong, L., *A discrete stochastic model of the COVID-19 outbreak: Forecast and control*, Mathematical Biosciences and Engineering 17.**4** (2020), pp. 2792–2804, doi:10.3934/mbe.2020153.

[21] Libotte, G. B., Lobato, F. S., and Platt, G. M., *Identification of an Epidemiological Model to Simulate the COVID-19 Epidemic using Robust Multi-objective Optimization and Stochastic Fractal Search*, arXiv:2006.00289, 2020, https://arxiv.org/abs/2006.00289.

[22] Le Strat, Y. and Carrat, F., *Monitoring epidemiologic surveillance data using hidden Markov models*, Statistics in Medicine 18.**24** (1999), pp. 3463–3478, doi:10.1002/(SICI)1097-0258(19991230)18:24<3463::AID-SIM409>3.0.CO;2-I.

[23] Rihan, F. A., Alsakaji, H. J., and Rajivganthi, C., *Stochastic SIRC epidemic model with time-delay for COVID-19*, Advances in Difference Equations 2020 (2020), p. 502, doi:10.1186/s13662-020-02964-8.

[24] Southall, E., Brett, T. S., Tildesley, M. J., and Dyson, L., *Early warning signals of infectious disease transitions: a review*, Journal of the Royal Society Interface 18.**182** (2021), p. 20210555, doi:10.1098/rsif.2021.0555.

[25] Polanco-González, C., Castañón-González, J. A., Buhse, T., Samaniego-Mendoza, J. L., Arreguín-Nava, R., and Villanueva-Martínez, S., *[Modified overcrowd index in emergency room]*, Gaceta Médica de México 149.**4** (2013), Artículo en español, pp. 417–424.

[26] Marc, A. et al., *Viral Dynamic Models During COVID-19: Are We Ready for the Next Pandemic?*, CPT: Pharmacometrics & Systems Pharmacology 14.**8** (Aug. 2025), pp. 1289–1297, doi:10.1002/psp4.70055.

Spiral RF Coil Analytical Modeling for Ultra-Low Field MRI Applications

Sergio Enrique Solís Nájera

Short Note

Received: 15 October 2026

Accepted: 02 November 2026

Published: 04 November 2026

DOI: 10.5281/zenodo.24047654

MSC 2020: 78A25

Published in RandPunkt Journal under the CC BY 4.0 license.

RandPunkt
Journal

ISSN 00009172 (Online)
APPLIED MATHEMATICS SERIES

Spiral RF Coil Analytical Modeling for Ultra-Low Field MRI Applications

Sergio Enrique Solís Nájera[1]

[1] *Departamento de Física, Facultad de Ciencias, UNAM, Ciudad de México*

*Correspondence to: **Sergio Enrique Solís Nájera** ▪ solisnajera@ciencias.unam.mx

Volume 1, Issue 1, 2026
Published on: 4 November 2026

Pages: [1–6] ▪ 6 pages
Article DOI: 10.5281/zenodo.24047654

Abstract. This study presents the analytical derivation and mathematical modeling of the quasi-static magnetic field produced by a spiral radiofrequency (RF) coil, designed for an ultra-low field magnetic resonance imaging (MRI) system operating at a Larmor frequency of 11.71 MHz. The model is constructed using the Biot–Savart law, approximating the RF coil as the superposition of eight concentric rectangular loops based on the physical dimensions of a fabricated prototype. A closed-form expression for the on-axis magnetic field is derived and numerically evaluated.

Keywords: Ultra Low Magnetic Field • Spiral RF Coil • analytical model

1 Introduction

Radiofrequency (RF) coils in magnetic resonance imaging (MRI) act as transducers responsible for transmitting excitation pulses and receiving the resulting nuclear magnetic resonance (NMR) signals [1, 2]. Recently, ultra-low field MRI systems have gained significant traction due to their portability, lower cost, and compatibility with metallic implants. In these systems, the RF coil must generate a highly homogeneous oscillating magnetic field (B_1) over the region of interest. Coil performance is typically characterized by the magnitude of the generated magnetic field as a function of penetration depth. Among various geometries, the **spiral coil** has demonstrated excellent performance and has been successfully implemented in high magnetic field MRI [3, 4] and low magnetic field applications [5].

The primary objective of this work is to derive a step-by-step, closed-form mathematical model to calculate the magnetic field H (A/m) produced by this specific spiral geometry.

Received: 15 October 2026 ▪ Accepted: 2 November 2026 ▪ Published: 4 November 2026 © 2026 CC by ▪ 4.0v

1.1 Spiral Coil Description

The model is based on a constructed spiral RF coil using 21 AWG copper wire (nominal diameter $d_w \approx 0.72$ mm), wound over a rigid template shaped as a rectangle with rounded corners. The coil consists of a total of 8 turns, organized into two distinct groups:

- **Group A (Turns 0 to 4):** Concentric turns wound contiguously (tightly packed), where each turn is in direct physical contact with the adjacent one.
- **Group B (Turns 5, 6, and 7):** Inner turns featuring a larger winding pitch.

The design operating frequency is $f = 11.71$ MHz. Each turn n is modeled as a rectangle, characterized by its half-width w_n and half-length l_n (half of the total measured width × length dimensions). Table 1 summarizes the dimensions measured directly on the fabricated coil.

Turn n	Width × Length (mm)	w_n (mm)	l_n (mm)
0 (outer)	28×38.8	14.0	19.4
1	26×36.0	13.0	18.3
2	24×33.0	12.0	17.2
3	22×30.0	11.0	16.1
4	20×30.0	10.0	15.0
5	14×24.0	7.0	12.0
6	10×18.0	5.0	9.0
7 (inner)	6×12.0	3.0	6.0

Table 1. Measured dimensions of each turn of the rounded spiral coil. The half-width (w_n) and half-length (l_n) are used in the analytical model.

The pitch of ≈ 1.0 mm observed in the first five transitions matches, within the expected manufacturing tolerance, the physical diameter of the wire (0.72 mm). This **geometrically confirms** that these turns are wound contiguously, consistent with the physical description of Group A. The larger pitch in the final two transitions is consistent with the wider spacing of Group B.

2 Magnetic Field Generation: Theoretical Framework

2.1 Quasi-Static Regime

The free-space wavelength at the operating frequency is:

$$\lambda = \frac{c}{f} = \frac{3 \times 10^8 \text{ m s}^{-1}}{11.71 \times 10^6 \text{ Hz}} \approx 25.6 \text{ m} \tag{1}$$

Since the physical dimensions of the coil (on the order of centimeters) are significantly smaller than λ, propagation delay across the coil can be neglected. The problem can therefore be treated within the **quasi-static (magnetostatic) regime**: the current $I(t) = I_0 \cos(\omega t)$ is assumed to be uniform in magnitude across the entire winding at any given instant, and the spatial field is calculated using the standard Biot–Savart law:

$$\vec{H}(\vec{r},t) = \vec{H}_{BS}(\vec{r})\,\cos(\omega t), \qquad \omega = 2\pi f. \tag{2}$$

Due to the electrically small size of the coil, the Biot–Savart law is highly appropriate for calculating the B_1 field of this RF coil.

2.2 Field of a Finite Current Segment

The fundamental building block of the model is the field generated by a straight finite current segment I. For an observation point P at a perpendicular distance d from the line containing the segment, with angles α_1 and α_2 subtended at the endpoints:

$$\vec{H} = \frac{I}{4\pi d}\,(\cos\alpha_1 - \cos\alpha_2)\,\hat{n}, \tag{3}$$

where $\hat{n}$ is the unit vector perpendicular to the plane formed by the segment and P (determined by the right-hand rule). This expression is obtained by directly integrating the differential form of the Biot–Savart law,

$$d\vec{H} = \frac{I}{4\pi}\frac{d\vec{l}\times\hat{r}}{r^2}, \tag{4}$$

along the segment. This approach is utilized because any polygonal geometry—such as a rectangle with rounded corners—can be decomposed into a finite number of straight segments (and arcs for the corners). By the superposition principle, the total field is the vector sum of the contributions from each segment.

2.3 Derivation of the Axial Field for a Rectangular Loop

To obtain a closed-form expression (avoiding the numerical summation of dozens of segments), we derive the specific case of the field **on the axis of symmetry** of a rectangular loop. This will subsequently be used as an approximation for each turn of the coil (neglecting the corner rounding, which is a second-order correction).

Consider a rectangular loop centered at the origin in the xy-plane, with half-width w (side parallel to the x-axis, from $-w$ to w) and half-length l (side parallel to the y-axis, from $-l$ to l). We seek $\vec{H}$ at the axial point $P = (0, 0, z)$.

Contribution of a single side. Consider the side at $y = l$, $z = 0$, with current flowing in the $+\hat{x}$ direction. A current element at $(x, l, 0)$ contributes:

$$d\vec{H} = \frac{I}{4\pi r^3}\,dx\,\hat{x}\times\vec{r}, \qquad \vec{r} = (-x, -l, z), \quad r = \sqrt{x^2 + l^2 + z^2}. \tag{5}$$

Evaluating the cross product, $\hat{x}\times\vec{r} = -l\,\hat{z} - z\,\hat{y}$, such that the axial component is:

$$dH_z = -\frac{I\,l}{4\pi}\,\frac{dx}{(x^2 + l^2 + z^2)^{3/2}}. \tag{6}$$

Integration over the side. Integrating x from $-w$ to w, and defining $c^2 \equiv l^2 + z^2$, we use the standard integral $\int dx/(x^2+c^2)^{3/2} = x/\left(c^2\sqrt{x^2+c^2}\right)$:

$$H_z^{(\text{side})} = -\frac{I\,l}{4\pi} \cdot \frac{2w}{(l^2+z^2)\sqrt{w^2+l^2+z^2}}. \tag{7}$$

Symmetry of the four sides. The opposite side ($y = -l$) carries current in the $-\hat{x}$ direction and, by symmetry, contributes with the same effective sign. When we sum both sides parallel to the x-axis, the factor of 2 that comes from adding the two identical contributions is already absorbed into the following expression:

$$H_z^{(x\text{-sides})} = \frac{I\,w\,l}{\pi\,(l^2+z^2)\sqrt{w^2+l^2+z^2}}. \tag{8}$$

By the same procedure, interchanging $w \leftrightarrow l$, the two sides parallel to the y-axis (at $x = \pm w$) contribute:

$$H_z^{(y\text{-sides})} = \frac{I\,w\,l}{\pi\,(w^2+z^2)\sqrt{w^2+l^2+z^2}}. \tag{9}$$

Closed-form result. Summing the contributions from the four sides yields:

$$H_z(z) = \frac{I\,w\,l}{\pi\sqrt{w^2+l^2+z^2}}\left[\frac{1}{l^2+z^2} + \frac{1}{w^2+z^2}\right] \tag{10}$$

Decomposing the loop into its four straight sides allows the exact application of the finite segment formula (Eq. 3) to each segment. Furthermore, the spatial symmetry of the problem ($x \to -x$, $y \to -y$) guarantees that only the H_z component survives on the axis, significantly simplifying the algebra.

3 Complete Analytical Model of the Rounded Spiral Coil

The coil is approximated as the superposition of $N = 8$ concentric rectangular loops (one per turn), each with its respective (w_n, l_n) from Table 1. By the superposition principle (all turns carry the same current I_0, as it is a series winding and the quasi-static approximation holds):

$$H_z(z) = I_0 \sum_{n=0}^{7} \frac{w_n\,l_n}{\pi\sqrt{w_n^2+l_n^2+z^2}}\left[\frac{1}{l_n^2+z^2} + \frac{1}{w_n^2+z^2}\right] \tag{11}$$

where w_n, l_n, and z must be expressed in meters to obtain H_z in A/m.

4 Numerical evaluation

The analytical model (Eq. 11) calculates the field strictly on the *axis of symmetry*, which is equidistant from all 8 turns and represents the point of *lowest* field intensity within the plane of the spiral RF coil. At $z = 0$, precisely at the *surface of the conductor*, the field is dominated by the near-field of each individual conductor segment. Evaluating Eq. 11 with an excitation current of $I_0 = 1$ A for $z \in [0, 50]$ mm yields the data presented in Figure 1. Also, a contour map at 3 different values of z was obtained (Figure 2).

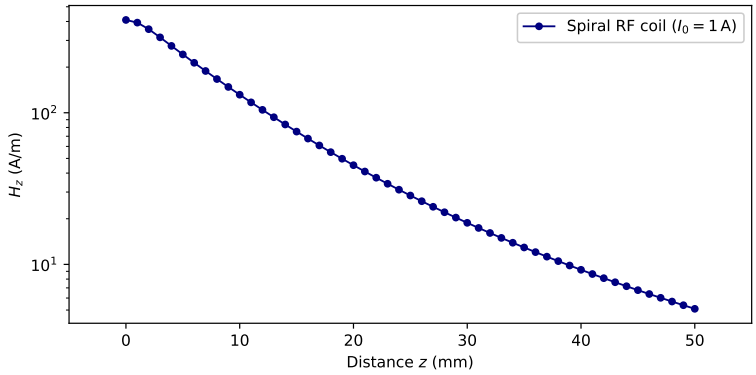


Figure 1. Axial magnetic field $H_z(z)$ of the 8-turn analytical model on a logarithmic scale.

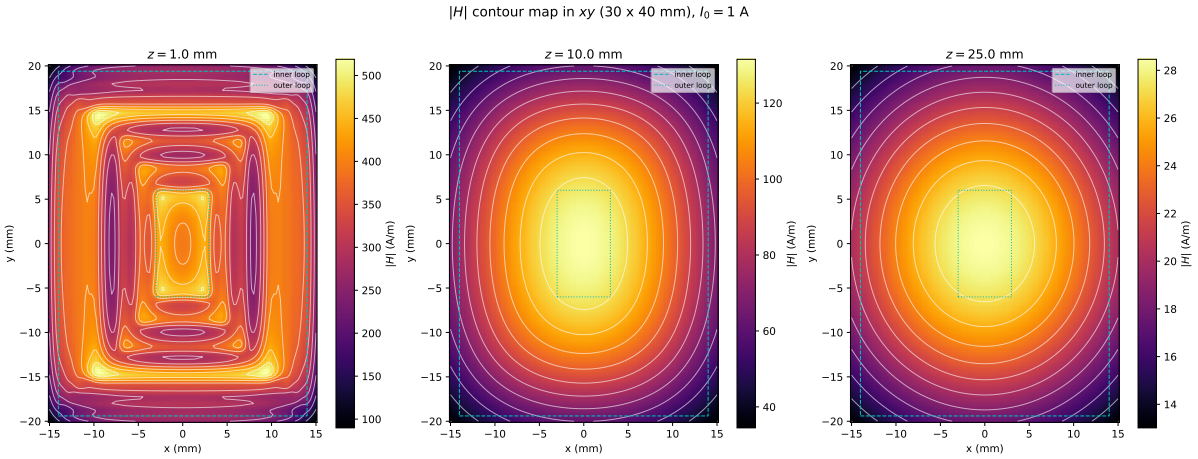


Figure 2. Axial magnetic field $H_z(z)$ contour maps for $I_0 = 1$ A at different z values.

The maximum field, located at the center of the coil ($z = 0$), is approximately 409.279 A/m per ampere of excitation current. For a single segment at its surface ($r \approx 0.36$ mm, $I = 1$ A), this yields $H \approx 441$ A/m. With 8 tightly packed turns (pitch ≈ 0.7 mm), the sum of their near-fields is on the order of 400 A/m. Furthermore, at 11.71 MHz, the skin depth in copper is $\delta \approx 19$ μm wire radius. Consequently, the current concentrates on the surface and edges of the conductor (particularly at the corners), generating local field hotspots that are significantly more intense than the uniform filamentary average assumed in the analytical model. Full 3D electromagnetic simulations are therefore required to accurately capture these proximity and skin effects.

5 Conclusions

In this work, a closed-form analytical model for the axial magnetic field of a rounded spiral RF coil was derived from first principles (Biot–Savart law). The physical geometry of the model was rigorously validated against direct physical measurements of a fabricated prototype, confirming that the winding pitch of the outer turns matches the wire diameter. The analytical model predicts a maximum on-axis field of 409.3 A/m per ampere at the coil center, exhibiting a rapid, monotonic decay as the distance from the coil plane increases. Finally, the comparison with electromagnetic simulations highlights the physical boundaries of the filamentary current assumption, demonstrating that while the analytical model is highly

effective for far-field and on-axis approximations, full-wave simulations are necessary to account for near-field surface effects, skin depth, and current crowding at the conductor boundaries.

Acknowledgements

The authors thank the anonymous referees for valuable comments that improved the presentation of this work.

References

[1] Vaughan, J. T. and Griffiths, J. R., *RF Coils for MRI*, 1st ed., United Kingdom: John Wiley & Sons, 2012.

[2] Jin, J., *Electromagnetic Analysis and Design in Magnetic Resonance Imaging*, New York: CRC Press, 1999.

[3] Motovilova, E., Sandeep, S., Hashimoto, M., and Huang, S. Y., *Water-Tunable Highly Sub-Wavelength Spiral Resonator for Magnetic Field Enhancement of MRI Coils at 1.5 T*, IEEE Access 7 (2019), pp. 90304–90315, doi:10.1109/ACCESS.2019.2927359.

[4] Woo, D.-C., Choe, B.-Y., Ha, S.-H., and Choi, C.-B., *Evaluation of the turn variation of spiral RF surface coils for MR microscopic imaging and spectroscopy*, Measurement 40.**6** (2007), pp. 615–622, doi:10.1016/j.measurement.2006.09.006.

[5] Díaz-Díaz, F., Cano-Barrita, P., León-Martínez, F., and Acevedo-Arzola, V., *1H NMR Sensor for Nondestructive Characterization of Organic and Inorganic Materials*, Sensors 24.**23** (2024), p. 7692, doi:10.3390/s24237692.

A Mathematical Framework for Predicting the Location and Extent of Complex Cardiac Ruptures

Francisco Javier Roldan Gomez

Short Note

Received: 15 October 2026

Accepted: 02 November 2026

Published: 04 November 2026

DOI: 10.5281/zenodo.24047363

MSC 2020: 92C10

Published in RandPunkt Journal under the CC BY 4.0 license.

RandPunkt
Journal

ISSN 00009172 (Online)
APPLIED MATHEMATICS SERIES

A Mathematical Framework for Predicting the Location and Extent of Complex Cardiac Ruptures

Francisco Javier Roldán Gómez[1]

[1] *Departamento de Consulta Externa, Instituto Nacional de Cardiología Ignacio Chávez, Mexico City 14080, Mexico*

*Correspondence to: **Francisco Javier Roldán Gómez** ▪ roldan@cardiologia.org.mx

Volume 1, Issue 1, 2026 **Pages:** [1 – 3] ▪ 3 pages
Published on: 4 November 2026 Article DOI: 10.5281/zenodo.24047363

Cardiac rupture after myocardial infarction is a high-mortality complication whose spatial pattern remains poorly predicted [1]. This note argues that the appropriate mathematical framework is anisotropic computational fracture mechanics, specifically the coupling of finite element analysis with a crack phase-field model that incorporates myocardial fiber orientation [2]. The clinical observation that dissection paths originate where the components of the helical ventricular myocardial band converge suggests a geometric and material discontinuity, which we formalize as a weak interface in a fibrous continuum [1]. We identify the mathematical objects involved: an anisotropic hyperelastic constitutive law, a phase-field variable governed by an energy-based anisotropic criterion, and a finite element discretization that resolves the fiber field from diffusion tensor imaging [3]. The result is a field theory of material failure that predicts a rupture surface rather than a probability, and it constitutes the natural mathematical extension of the author's clinical research line.

Keywords: anisotropic fracture; crack phase-field; cardiac rupture; finite element analysis; myocardial fiber architecture; intramyocardial dissection.

1 The mathematical object

The clinical problem is stated geometrically: given a ventricular domain $\Omega \subset \mathbb{R}^3$ with a known infarct region $\Omega_{\text{inf}} \subset \Omega$, predict the initiation site and propagation path of a rupture [1]. The relevant mathematical object is not a scalar risk score but a *vector field of material failure*, defined on the same domain that carries the stress state.

Received: 15 October 2026 ▪ Accepted: 2 November 2026 ▪ Published: 4 November 2026 © 2026 CC by ▪ 4.0v

The passive myocardium is modeled as a fiber-reinforced hyperelastic continuum. Let $\mathbf{F}$ be the deformation gradient and $\mathbf{C} = \mathbf{F}^{\top}\mathbf{F}$ the right Cauchy–Green tensor. The strain energy is decomposed as

$$\Psi = \Psi_{\text{iso}}(\mathbf{C}) + \sum_{i=\text{f,s}} \Psi_{\text{aniso}}(\mathbf{C}, \mathbf{a}_i \otimes \mathbf{a}_i), \tag{1}$$

where $\mathbf{a}_{\text{f}}$ and $\mathbf{a}_{\text{s}}$ are the fiber and sheetlet directions obtained from diffusion tensor imaging tractography [3]. This is the standard constitutive foundation for cardiac finite element models [4].

The rupture itself is described by a *phase-field variable* $d : \Omega \to [0, 1]$, where $d = 0$ denotes intact tissue and $d = 1$ fully fractured material. The total energy functional is

$$\mathcal{E}(\mathbf{u}, d) = \int_{\Omega} \Psi(\mathbf{C})\, \mathrm{d}V + \int_{\Omega} G_c\, \gamma(d, \nabla d)\, \mathrm{d}V, \tag{2}$$

where G_c is the fracture toughness and γ is the crack surface density function [2]. The critical point of (2) yields the coupled displacement–damage problem.

2 The anisotropic criterion

The essential mathematical ingredient for this specific clinical problem is *anisotropy of the fracture criterion*. In an isotropic phase-field model, the crack path is determined solely by the stress field. In the myocardium, the fiber architecture biases propagation: a crack oriented parallel to the fibers requires less energy than one crossing them [2].

The energy-based anisotropic criterion replaces the scalar G_c by a directional fracture toughness $G_c(\mathbf{n})$, where $\mathbf{n}$ is the crack normal. A tractable form is

$$G_c(\mathbf{n}) = G_{c,\perp} + (G_{c,\parallel} - G_{c,\perp})\, (\mathbf{n} \cdot \mathbf{a}_{\text{f}})^2, \tag{3}$$

with $G_{c,\parallel} < G_{c,\perp}$ reflecting the experimentally observed preference for fiber-parallel splitting [2]. Substituting (3) into (2) yields a phase-field evolution equation whose minimizers are crack paths that align with the local fiber direction.

This is precisely the mathematical mechanism required to formalize the clinical hypothesis: the "convergence of three components" described in the clinical report of Vargas et al. [1] corresponds to a region where $\mathbf{a}_{\text{f}}$ rotates rapidly, so that the directional toughness (3) varies steeply in space. Within this formulation, such a region is expected to act as a *geometric attractor* for the phase-field: because $G_c(\mathbf{n})$ varies steeply there, the phase-field evolution is biased toward concentrating damage and initiating the dissection path along that interface. In this note, *dissection path* and *rupture surface* are used interchangeably: the phase-field level set $d = 1$ is a two-dimensional surface in Ω, whose intersection with the endocardium traces the clinically observed dissection path.

3 The computational realization

The anisotropic criterion (3) is discretized together with (2) as follows. The displacement field $\mathbf{u}$ and the phase-field d are approximated on a mesh $\mathcal{T}_h$ of the ventricular geometry, reconstructed from magnetic resonance imaging. The fiber directions $\mathbf{a}_{\text{f}}$ are interpolated from diffusion tensor tractography data [3], which provides the spatial field of myocardial architecture at resolutions of the order of a few hundred micrometers—sufficient to resolve the transmural fiber rotation.

The coupled system is solved incrementally under ventricular pressure loading, with the infarct region assigned degraded material properties consistent with scar tissue [4]. The output is a spatiotemporal field $d(\mathbf{x}, t)$ whose level sets trace the predicted dissection surface.

A historical precedent supports this choice: Reif and Silver [4] used a finite element model of the infarcted left ventricle to show that maximum von Mises stress concentrates at the endocardial surface near the infarct border, and proposed the pathogenic sequence *stress concentration* → *endocardial tear* → *dissecting hemorrhage*. The phase-field formulation extends that static stress analysis into a predictive theory of *where the tear propagates*.

4 Outlook

The mathematical line established in this note is anisotropic crack phase-field modeling coupled with finite element analysis of the fiber-reinforced myocardium [2, 4]. This framework formalizes the clinical research line pursued by the author. Specifically, the convergence of the three components of the helical ventricular myocardial band documented in [1] corresponds to a region of rapid fiber rotation, which in the model appears as a steep spatial gradient of directional toughness $G_c(\mathbf{n})$; the dissection paths observed clinically are then predicted as minimizers of the phase-field functional in that region. The output of the framework is therefore a predicted rupture surface on the ventricular domain, not a scalar probability.

References

[1] Vargas-Barrón, J., Roldán, F.-J., Romero-Cárdenas, Á., and Vázquez-Antona, C.-A., *Intramyocardial Dissecting Hematoma and Postinfarction Cardiac Rupture*, Echocardiography 30.**1** (2013), PMID: 23167290, pp. 106–113, doi:10.1111/echo.12017.

[2] Gültekin, O., Hager, S. P., Dal, H., and Holzapfel, G. A., *Computational Modeling of Progressive Damage and Rupture in Fibrous Biological Tissues: Application to Aortic Dissection*, Biomechanics and Modeling in Mechanobiology 18.**6** (2019), PMID: 31093869; PMCID: PMC6825033, pp. 1607–1628, doi:10.1007/s10237-019-01164-y.

[3] Poveda, F., Gil, D., Martí, E., Andaluz, A., Ballester, M., and Carreras, F., *Helical Structure of the Cardiac Ventricular Anatomy Assessed by Diffusion Tensor Magnetic Resonance Imaging With Multiresolution Tractography*, Revista Española de Cardiología (English Edition) 66.**10** (2013), PMID: 24773858, pp. 782–790, doi:10.1016/j.rec.2013.04.021.

[4] Reif, T. H. and Silver, M. D., *Role of Stress Concentration in the Pathogenesis of Cardiac Rupture Following Acute Myocardial Infarction*, Canadian Journal of Cardiology 11.**9** (1995), Not indexed in PubMed; available via journal archive, pp. 757–762.

Mathematical Structure of the Nonheme Iron Determination Assay

Alberto Huberman

Short Note

Received: 15 October 2026

Accepted: 02 November 2026

Published: 04 November 2026

DOI: 10.5281/zenodo.24041134

MSC 2020: 92C40

Published in RandPunkt Journal under the CC BY 4.0 license.

RandPunkt
Journal

ISSN 00009172 (Online)
APPLIED MATHEMATICS SERIES

Mathematical Structure of the Nonheme Iron Determination Assay

Alberto Huberman[1]

[1] *Instituto Nacional de Ciencias Médicas y Nutrición "Salvador Zubirán", Department of Biochemistry, Vasco de Quiroga 15, Tlalpan, Mexico City 14000, Mexico*

*Correspondence to: **Alberto Huberman** ▪ amhuber@unam.mx

Volume 1, Issue 1, 2026 **Pages:** [1 – 3] ▪ 3 pages
Published on: 4 November 2026 Article DOI: 10.5281/zenodo.24041134

The nonheme iron determination micromethod of Huberman and Pérez [1] is recast as a linear calibration problem. We show that the assay is governed by the affine predictor $\hat{c} = (A - \hat{b}_0)/\hat{m}$, derived from the Beer–Lambert law [2, 3] and estimated by ordinary least squares [4]. Around this predictor we identify three mathematical objects: an uncertainty functional [5, 6], a dilution factor, and a decision rule [7]. Their composition yields a predictive map Φ that converts absorbance into concentration, interval, and clinical label. The note argues that this mathematical profile, rather than the chemical procedure, is what makes the assay portable and automatable in low-resource laboratories.

Keywords: linear calibration; Beer–Lambert law; ordinary least squares; nonheme iron; predictive map; chemometrics.

1 The mathematical object

The micromethod of Huberman and Pérez [1] quantifies nonheme iron spectrophotometrically. Its physical basis is the Beer–Lambert law [2, 3],

$$A = \varepsilon\, b\, c, \tag{1}$$

where A is absorbance, ε the molar absorptivity, b the optical path, and c the concentration. Since εb is constant for a given setup, (1) is a linear relation between A and c. The assay is therefore a *linear calibration problem* [4]:

$$A_i = m\, c_i + b_0 + \varepsilon_i, \qquad i = 1, \ldots, n, \tag{2}$$

Received: 15 October 2026 ▪ Accepted: 2 November 2026 ▪ Published: 4 November 2026 © 2026 CC by ▪ 4.0v

with sensitivity $m = \varepsilon b$, intercept b_0, and error ε_i. The ordinary least-squares estimates are [4, 8]

$$\hat{m} = \frac{\sum_i (c_i - \bar{c})(A_i - \bar{A})}{\sum_i (c_i - \bar{c})^2}, \qquad \hat{b}_0 = \bar{A} - \hat{m}\,\bar{c}. \tag{3}$$

In the two-standard version of the original method [1] ($c_1 = 100$, $c_2 = 10$ μg/mL), (3) reduces to a straight line through two points. In either case, the concentration of an unknown sample is the affine predictor

$$\boxed{\hat{c} = \frac{A_{\text{sample}} - \hat{b}_0}{\hat{m}}} \tag{4}$$

This is the mathematical core of the assay: a function from optical signal to concentration. It is the simplest affine model consistent with (1), and it is exact whenever the calibration is exact [9].

2 Three derived objects

The predictor (4) is not yet a usable tool. Three mathematical objects complete it.

First, the *uncertainty functional*. Assuming the standard conditions for linear regression—namely, that the errors ε_i are independent, normally distributed, and homoscedastic (constant variance)—we can apply first-order propagation [5, 6] to obtain:

$$\sigma_c^2 = \frac{\sigma_A^2}{\hat{m}^2} + \frac{\sigma_m^2\,(A - \hat{b}_0)^2}{\hat{m}^4} + \frac{\sigma_{b_0}^2}{\hat{m}^2}, \tag{5}$$

which yields the interval $\hat{c} \pm t_{n-2,1-\alpha/2}\,\sigma_c$ and the analytical limits $\text{LOD} = 3.3\,\sigma_{b_0}/\hat{m}$, $\text{LOQ} = 10\,\sigma_{b_0}/\hat{m}$ [10, 11].

Second, the *dilution factor* $F_d = V_{\text{final}}/V_{\text{aliquot}}$, so that the true concentration is $c_{\text{real}} = \hat{c}\,F_d$. This is the algebra behind the 1:10 secondary standard of the original note [1].

Third, the *decision rule* [7, 12]

$$D(\hat{c}) = \begin{cases} \text{deficient}, & \hat{c} < c_{\text{threshold}}, \\ \text{normal}, & \hat{c} \geq c_{\text{threshold}}. \end{cases} \tag{6}$$

3 The predictive map

Composing the three objects with (4) gives the predictive map

$$\Phi(A) = \big(c_{\text{real}}(A),\ \sigma_c(A),\ D(c_{\text{real}}(A))\big), \tag{7}$$

with $c_{\text{real}}(A) = \frac{A - \hat{b}_0}{\hat{m}} F_d$. The user enters an absorbance and receives a concentration, an interval, and a clinical label. Because the map Φ reduces the entire calculation to a single algebraic step, it is what allows the method to be implemented portably and automatically on a spreadsheet, without specialized software.

The same construction extends to multivariate calibration. If several wavelengths, replicates, pH, or temperature are recorded, (2) becomes a multiple linear regression whose matrix solution is $\hat{\boldsymbol{\beta}} = (\mathbf{X}^\top \mathbf{X})^{-1} \mathbf{X}^\top \mathbf{A}$ [13, 9], the natural bridge to chemometrics [14, 15].

4 Outlook

The nonheme iron assay admits a compact mathematical profile organized around the affine predictor (4) and the predictive map (7). The disciplines that sustain it are applied statistics and chemometrics [14, 15], supported by linear algebra [13, 9], error propagation, and decision theory [7]. Framing the method in these terms does not replace the chemical procedure [1]; rather, this formalization aims to make it reproducible and usable by non-specialists, which is precisely the setting for which the micromethod was designed.

References

[1] Huberman, A. and Pérez, C., *Nonheme iron determination*, Notes & Tips (2001), Instituto Nacional de Ciencias Médicas y Nutrición "Salvador Zubirán", Department of Biochemistry, Mexico City.

[2] Ingle, J. D. and Crouch, S. R., *Spectrochemical Analysis*, Upper Saddle River, NJ: Prentice Hall, 1988.

[3] Harris, D. C., *Quantitative Chemical Analysis*, 9th ed., New York: W. H. Freeman, 2015.

[4] Montgomery, D. C., Peck, E. A., and Vining, G. G., *Introduction to Linear Regression Analysis*, 5th ed., Hoboken, NJ: Wiley, 2012.

[5] Bevington, P. R. and Robinson, D. K., *Data Reduction and Error Analysis for the Physical Sciences*, 3rd ed., New York: McGraw-Hill, 2003.

[6] Taylor, J. R., *An Introduction to Error Analysis: The Study of Uncertainties in Physical Measurements*, 2nd ed., Sausalito, CA: University Science Books, 1997.

[7] Berger, J. O., *Statistical Decision Theory and Bayesian Analysis*, 2nd ed., New York: Springer, 1985.

[8] Draper, N. R. and Smith, H., *Applied Regression Analysis*, 3rd ed., New York: Wiley, 1998.

[9] Strang, G., *Introduction to Linear Algebra*, 5th ed., Wellesley, MA: Wellesley-Cambridge Press, 2016.

[10] Currie, L. A., *Limits for qualitative detection and quantitative determination: Application to radiochemistry*, Analytical Chemistry 40.**3** (1968), pp. 586–593, doi:10.1021/ac60259a007.

[11] Thompson, M., Ellison, S. L. R., and Wood, R., *Harmonized guidelines for single-laboratory validation of methods of analysis (IUPAC Technical Report)*, Pure and Applied Chemistry 74.**5** (2002), pp. 835–855, doi:10.1351/pac200274050835.

[12] Hastie, T., Tibshirani, R., and Friedman, J., *The Elements of Statistical Learning: Data Mining, Inference, and Prediction*, 2nd ed., New York: Springer, 2009.

[13] Golub, G. H. and Van Loan, C. F., *Matrix Computations*, 4th ed., Baltimore: Johns Hopkins University Press, 2013.

[14] Massart, D. L., Vandeginste, B. G. M., Buydens, L. M. C., De Jong, S., Lewi, P. J., and Smeyers-Verbeke, J., *Handbook of Chemometrics and Qualimetrics: Part A*, Amsterdam: Elsevier, 1997.

[15] Brereton, R. G., *Chemometrics: Data Analysis for the Laboratory and Chemical Plant*, Chichester: Wiley, 2003.